UNIVERSIDAD NACIONAL AUTÓNOMA DE MÉXICO
PROGRAMA DE POSGRADO EN ASTROFÍSICA
Instituto de Radioastronomía y Astrofísica

CAMPOS MAGNÉTICOS EN LA FORMACIÓN DE NUBES EN EL MEDIO INTERESTELAR

PARA OPTAR POR EL GRADO DE
DOCTOR EN CIENCIAS (ASTROFÍSICA)

PRESENTA

GUIDO ELAR GRANDA MUÑOZ

TUTORES
DR. ENRIQUE VÁZQUEZ SEMADENI
INSTITUTO DE RADIOASTRONOMÍA Y ASTROFÍSICA

DR. GILBERTO GÓMEZ REYES
INSTITUTO DE RADIOASTRONOMÍA Y ASTROFÍSICA

Morelia, Michoacán, México

Marzo, 2023

Institute of
Radio Astronomy and Astrophysics
National Autonomous University of Mexico

Ph.D. Thesis

Magnetic fields in the formation of clouds in the interstellar medium

Guido Elar Granda Muñoz

NATIONAL AUTONOMOUS UNIVERSITY OF MEXICO
POSGRADUATE PROGRAM IN ASTROPHYSICS
Institute of Radioastronomy and Astrophysics

Supervisors:
Dr. Enrique Vázquez Semadeni
Dr. Gilberto Gómez Reyes

Magnetic fields in the formation of clouds in the interstellar medium

Ph.D. thesis

by

Guido Elar Granda Muñoz

Supervisors: Dr. Enrique Vázquez Semadeni
Dr. Gilberto Gómez Reyes

Institute of
Radio Astronomy and Astrophysics
National Autonomous University of Mexico

Abstract

In this Ph.D. thesis, we study two aspects of the magnetic interstellar medium. The first is a numerical resolution criterion for resolving magnetic fields in simulations of molecular clouds, and the second is the alignment of the magnetic field with cold atomic clouds.

The resolution criterion consists in finding the numerical resolution at which dynamical time relevant for the evolution of the molecular cloud is larger than the magnetic diffusion time, where the magnetic diffusion time is obtained by previously computing the numerical magnetic diffusion coefficient employing a numerical experiment.

For the case of subcritical clouds, we found that insufficient numerical resolution results in a spurious gravitational collapse. However, when we apply our resolution criterion and obtain the numerical resolution at which the free-fall time is greater than the numerical magnetic diffusion time, the subcritical molecular cloud oscillates around an equilibrium state as expected.

To study the alignment of the magnetic field with density structures, we followed the evolution of the magnetic field lines in three-dimensional simulations of cloud formation by colliding flows with initial conditions typical of the interstellar medium. We found that the direction of the magnetic field lines changes at the shock front due to magnetohydrodynamic fast shocks. The passage of the shock front results in an initial magnetic field line pattern which is amplified by the downstream velocity field.

This amplification of the upstream magnetic field component parallel to the shock front, the amplification of the components of the magnetic field perpendicular to the original direction in the downstream region by the converging velocity field, and the drag of magnetic field lines results in the alignment of the magnetic field with density structures.

Resumen

En esta tesis de doctorado estudiamos dos aspectos del campo magnético en el medio interestelar. El primero es un criterio de resolución numérica del campo magnético para simulaciones de nubes moleculares y el segundo es el alineamiento del campo magnético con nubes de gas atómico frio.

El criterio de resolución propuesto consiste en encontrar la resolución numérica a la cual el tiempo de dinámico relevante para la evolución de la nube es mayor que el tiempo de difusión numérica del campo magnético en donde el tiempo de difusión es obtenido luego de calcular el coeficiente de difusión numérica del campo magnético mediante un experimento numérico.

En el caso de nubes subcríticas, encontramos que una resolución numérica insuficiente resulta en el colapso espurio de estas estructuras. Sin embargo, cuando aplicamos el criterio de resolución propuesto y obtenemos la resolución numérica a la cual el tiempo de caída libre es mayor que el tiempo de difusión del campo magnético la nube molecular subcrítica oscila alrededor del equilibrio como se espera.

En el estudio de la alineamiento del campo magnético con las estructuras de densidad seguimos la evolución de las lineas de campo magnético en simulaciones de formación de nubes por colisión de corrientes de gas atómico frío considerando condiciones iniciales típicas del medio interestelar. Hemos encontrado que la dirección de las lineas de campo magnético cambia en el frente de choque debido a la generación de un choque magnetohidrodinámico rápido. El paso del frente de choque resulta en un patrón inicial en las lineas de campo magnético el cual es amplificado por la velocidad corriente abajo.

La amplificación de la componente del campo magnético paralela al frente de choque debido al choque magnetohidrodiñamico rápido, la amplificación de las componentes del campo magnético perpendiculares a la orientación original y el arrastre de las lineas de campo magnético resulta en el alineamiento de las lineas de campo magnético con las estructuras de densidad.

Contents

Nomenclature

Abbreviations

Abbreviation	Definition
ISM	Interstellar medium
HIM	Hot ionized medium
WNM	Warm neutral medium
CNM	Cold neutral medium
TI	Thermal instability
MCs	Molecular clouds
GHD	Gravitational hydrodynamic
CACs	Cold atomic clouds
NTSI	Non-linear thin shell instability
HKI	Kelvin-Helmholtz instability
MHD	Magnetohydrodynamics
HD	Hydrodynamics
HRO	Histogram of relative orientations
MNRAS	Monthly notices of the royal astronomical society
AMR	Adaptive mesh refinement
MC7	Molecular cloud simulation of refinement level 7
MC8	Molecular cloud simulation of refinement level 8
MC9	Molecular cloud simulation of refinement level 9
H7	Harris-like simulation of refinement level 7
H8	Harris-like simulation of refinement level 8
H9	Harris-like simulation of refinement level 9
H10	Harris-like simulation of refinement level 10
H11	Harris-like simulation of refinement level 11

Variable Names

Symbol	Definition	Unit
T	Temperature	[K]

Symbol	Definition	Unit
n	Number density	[cm^{-3}]
n_H	Hydrogen number density	[cm^{-3}]
ρ	Volumetric density	[g cm^{-3}]
u	Velocity	[cm s^{-1}]
$u_{\rm A}$	Alfvén velocity	[cm s^{-1}]
t	Time	[s]
Λ	Cooling function	[erg s^{-1} cm^3]
Γ	Heating function	[erg s^{-1}]
W	Gravitational energy	[erg]
E_m	Magnetic energy	[erg]
C_m	Mass distribution and geometry constant	–
G	Gravitational constant	[cm^3 g^{-1} s^{-2}]
M	Mass	[g]
R	Radius	[cm]
B	Magnetic field	[G]
V	Volume	[cm^3]
Φ	Magnetic flux	[G cm^2]
$\hat{n}$	Normal unitary vector	–
A	Area	[cm^2]
μ	Mass to flux ratio	–
ϕ	Angle between the magnetic field and density gradient	[°]
d	Distance	[cm]
U	Gravitational potential	[cm^2 s^{-2}]
e	Internal energy per unit mass	[erg g^{-1}]
$F_{\rm L}$	Lorentz force	[dyn]
η	Magnetic diffusion coefficient	[cm^2 s^{-1}]
c	Speed of light	[cm s^{-1}]
σ_e	Electric conductivity	[g^{-1} cm^{-3} s^3 A^2]
$\tilde{\lambda}$	Particle mean free path	[cm]
$\hat{s}$	Normal to the shock front	–

Symbol	Definition	Unit
u_1	Upstream velocity	[cm s^{-1}]
u_2	Downstream velocity	[cm s^{-1}]
ρ_1	Upstream density	[g cm^{-3}]
ρ_2	Downstream density	[g cm^{-3}]
$\boldsymbol{B}_1$	Upstream magnetic field	[G]
$\boldsymbol{B}_2$	Downstream magnetic field	[G]
P_1	Upstream pressure	[dyn cm^{-2}]
P_2	Downstream pressure	[dyn cm^{-2}]
c_s	Sound speed	[cm s^{-1}]
P	Pressure	[dyn cm^{-2}]
γ	Heat capacity ratio	–
θ	Angle between the shock normal and the upstream magnetic field	[°]
$\mathcal{L}$	Total cooling function	[erg s^{-1}]
m_{H}	Atomic hydrogen mass	[g]
κ_ρ	Isothermal wave number	[cm^{-1}]
κ_T	Isochoric wave number	[cm^{-1}]
κ_K	Thermal conductivity wave number	[cm^{-1}]
ω	Growth rate	[s^{-1}]
$\tilde{\mu}$	Mean molecular weight	-
τ_s	Sound crossing time	[s]
τ_c	Cooling time	[s]
τ_{ff}	Free-fall time	[s]
τ_{A}	Alfvén crossing time	[s]
τ_d	Diffusion time	[s]
τ_{gt}	Thermal instability growth time	[s]
K	Thermal conductivity	[erg s^{-1} $cm^{-1}K^{-1}$]
k_{B}	Boltzmann constant	[erg K^{-1}]
λ	Wavelength of the perturbation	[cm]
$\tilde{k}$	Normalized wave number	–
Δ	Slab displacement	[cm]

Symbol	Definition	Unit
d	Slab thickness	[cm]
L_{J}	Jeans' length	[cm]
M_{J}	Jeans' mass	[g]
P_B	Magnetic pressure	[dyn cm^{-3}]
σ	Standard deviation	[cm]
M_{A}	Alfvénic Mach number	–
M_s	Mach number	–
ζ	Shape parameter	–
A_c	Central area	[cm^2]
A_e	External area	[cm^2]
u_f	Fast speed	[cm s^{-1}]
$u_{A,n}$	Alfvén speed normal component to the shock front	[cm s^{-1}]
$B_{\parallel,2}$	Downstream magnetic field component parallel to the shock front	[G]
$B_{\parallel,1}$	Upstream magnetic field component parallel to the shock front	[G]
$M_{A,1}$	Upstream Alfvénic mach number	–
r_ρ	Shock density ratio	–
B_x, B_y, B_z	Magnetic field components	[G]

1

Introduction

1.1. The Interstellar Medium (ISM)

The ISM is the matter and energy in between stars. It contains gas and dust spread inhomogeneously, cosmic rays, magnetic fields, and radiation from multiple sources. The presence of the ISM is detected by astronomers through obscuration, reddening, polarization of starlight, and the formation of absorption and emission spectra. The mass in the ISM is around $10-15\%$ of the mass of the Galactic disk and most of the ISM matter is concentrated in the Galactic plane and along the spiral arms where half of the interstellar matter is in clouds which occupy only $1-2\%$ of the interstellar volume (Ferrière, 2001). Therefore, understanding the physical processes in the ISM is crucial to elucidate how clouds and stars form.

According to Ferrière (2001), the ISM clouds can be divided into three types: dark, diffuse, and translucent clouds. Dark clouds are made of very cold gas ($T \sim 10-20$ K), molecular gas, and dust which blocks background radiation. Diffuse clouds are formed by cold atomic gas ($T \sim 100$ K) and they are almost transparent to background starlight. Translucent clouds contain atomic and molecular gas which yields a cloud with intermediate extinctions compared to dark and diffuse clouds.

The ISM is usually classified into different thermodynamic phases, which arise from physical processes such as ionizing photons, radiative cooling, recombination of ions and electrons, H_2 formation, etc. Initially, the ISM was considered as a two-phase medium in pressure equilibrium, one hot ($T = 10^4$ K) occupying most of the interstellar space, and one cold ($T < 300$ K) resulting from gravitational compression (Field et al., 1969). A few years later, McKee & Ostriker (1977) proposed that the ISM consists of three phases in pressure balance induced by supernova explosions. These phases are the hot ionized medium, the warm medium, and the cold phase.

The main feature of the two- and three-phase models of the ISM is that they rely on the concept of thermal and pressure equilibrium between their phases, i.e., phases with different densities and temperatures but with the same pressure. Therefore, unstable regimes were not considered in these models (Vázquez-Semadeni et al., 2003). In contrast, Gerola et al. (1974) introduce a time-dependent model for the ISM where stochastic local heating events caused strong fluctuations in density and temperature and as a consequence gas in an unstable regime. Afterward, Lioure & Chieze (1990) considered a model for the ISM with continuous gas recycling among the various phases of the ISM and concluded that a significant amount of gas should be unstable.

The hot ionized medium (HIM) originated by supernova explosions has temperatures $T > 10^6$ K and number densities $n \sim 10^{-2}$ cm^{-3}. The warm ionized medium (WIM) consists of low-density photoionized regions with $n \in [0.2, 0.5]$ cm^{-3} and $T \sim 8{\times}10^3$ K. The warm neutral medium (WNM) whose main component is neutral hydrogen (HI) has $T \in [6 \times 10^3, 10^4]$ K and hydrogen number density $n_H \sim 0.6$ cm^{-3}. The cold neutral medium (CNM) is mostly atomic gas with $T \in [50, 100]$ K and $n \approx 30$ cm^{-3} (Ferrière, 2001). All these phases of the ISM gas are compressible and subject to many physical processes that can change their properties and thermodynamic phase. The fluid equations describe how these physical processes affect the ISM because they describe the evolution of physical variables such as density, temperature, pressure, velocity, magnetic field, etc. These equations are usually solved numerically in simulations, but they are also useful to obtain approximated solutions with linear perturbation theory or other simplifications (see Section 2.1).

Regarding the equations of fluids, the energy conservation equation is essential because it includes cooling and heating mechanisms crucial for forming the different phases of the ISM. Cooling mechanisms release energy in form of radiation after the excitation of atoms and molecules while heating mechanisms give energy to the system.

The considered cooling mechanisms in the ISM convert kinetic energy into radiation after the collisional excitation of atoms and molecules followed by a radiative decay (Draine, 2011). The cooling function (Λ) includes these cooling processes and depends on the metallicity, ionization fraction, temperature, and radiation field of the region where the cooling takes place.

The principal heating mechanisms in the ISM are photo-ionization, cosmic ray heating, and photo-electric heating. Photo-ionization occurs when a photon ionizes an atom and the energy excess between the photon and the ionization potential constitutes the free electron's kinetic energy that contributes to the heating. Cosmic rays can remove electrons through collisions with atoms, molecules, and ions, further contributing to the heating. Photo-electric heating happens due to ejected electrons from dust grains with a kinetic energy excess. All these heating processes are included in the heating function (Γ) in the energy conservation equation.

1.2. Cloud Formation

The cooling and heating mechanisms present in the atomic ISM (Dalgarno & McCray, 1972; Wolfire et al., 1995) and mentioned in the previous section are responsible for the development of the thermal instability (TI), which is crucial for the formation of cold atomic and molecular clouds. The TI is the physical mechanism responsible for the formation of atomic clouds (Field, 1965) by the compression of the neutral medium (Hennebelle & Pérault, 2000; Koyama & Inutsuka, 2000) and implies the transition from the WNM to the CNM (See Section 2.3.1 for details).

Clouds in the ISM can be classified as atomic or molecular depending on the abundance of atomic or molecular gas. Therefore, the formation of molecular clouds (MCs), which constitute the densest, coldest regions in the ISM and the place for the formation and evolution of stars in our and nearby galaxies; must involve a transition from atomic to molecular gas.

The formation of cold atomic clouds (CACs) by colliding flows with pure hydrodynamic simulations, including the multi-phase nature of the ISM and not considering gravity nor

magnetic fields was studied by Heitsch et al. (2006). In this work, the authors discussed three important instabilities for the formation of CACs: the non-linear thin-shell instability (NTSI), the Kelvin-Helmholtz instability (KHI), and the already mentioned TI. These instabilities interacting with each other will give rise to the CACs (see section 2.3 for a description of these instabilities).

The main feature of the colliding gas flows forming CACs is its supersonic velocities, which lead to the formation of shocks. Shocks develop wherever there are supersonic relative velocities. Therefore, shocks are present in many places in the ISM besides the formation of clouds by supersonic colliding flows. For example, they can be caused by strong stellar winds, expanding H II regions, jets, outflows, colliding clouds, galactic density waves, and supernova explosions. Concerning the formation of clouds, simulations show that a shocked layer forms between the shock front and the condensation layer caused by the TI (e.g., Vázquez-Semadeni et al., 2006). The formation of shocks and their influence in the magnetic field is very important for the second part of this thesis (see Chapter 4) therefore we make a summary of the physics related to shocks in Section 2.2.

The physical mechanism that triggers the transition from atomic to molecular gas was unknown until recently. Originally, Kwan (1979) proposed that random coalescene of smaller clouds built them on times scales of the order of 10^8 years. Shortly thereafter, Blitz & Shu (1980) suggested that clump coalescence is sped up when the ISM is compressed while passing through a spiral arm in a galaxy, which reduces the star formation time to a few times 10^7 years for giant molecular clouds.

Later, compressible waves passing through the warm atomic diffusive medium and triggering a phase transition to the dense cold phase due to the TI were considered the responsible formation mechanism (e.g., Hennebelle & Pérault, 1999; Koyama & Inutsuka, 2000, 2002; Audit & Hennebelle, 2005; Heitsch et al., 2005, 2006; Vázquez-Semadeni et al., 2006). Afterward, the atomic gas becomes molecular through grain catalysis, a process through which a hydrogen atom becomes bound to the grain surface till a second hydrogen atom encounters it to form a hydrogen molecule (Draine, 2011). According to Franco & Cox (1986) and Hartmann et al. (2001), the cloud becomes gravitationally unstable when the column density in cold atomic clouds reaches the molecular threshold. This fact was also found by Vázquez-Semadeni et al. (2007) where the formation of molecular clouds due to the compression of the warm neutral medium (WNM) was simulated with gravitational hydrodynamic (GHD) simulations. Hence, cloud formation and evolution are also connected to support models, which propose a physical mechanism that might counteract gravitational collapse.

1.3. Support Models

Among cloud support models, quasi-stationary models consider that MCs and their substructures follow a quasi-stationary evolution due to support mechanisms against gravitational collapse. The most accepted quasi-stationary support models are the magnetic support model and the turbulent support model.

1.3.1. Magnetic Support Model

The standard magnetic support model assumes that the magnetic field controls the formation and evolution of molecular clouds because it provides support against gravitational collapse through the magnetic pressure gradient between molecular clouds and their surrounding medium (Shu et al., 1987; Mouschovias, 1991).

According to this model, molecular clouds that are born magnetically supported against gravitational collapse lose this support due to diffusive processes such as ambipolar diffusion (e.g., Mouschovias & Ciolek, 1999) and form low mass stars. In contrast, molecular clouds that are born without magnetic support form high mass stars.

The Mass-to-flux Ratio

The standard way to determine if magnetic fields are relevant to the molecular cloud support is to measure the mass-to-flux ratio. This quantity comes from the gravitational and magnetic energy ratio in molecular clouds. In order to compute the mass-to-flux ratio, the standard magnetic support model considers clouds as isolated structures, i.e., it neglects the surrounding mass and assumes that molecular clouds have a constant mass.

For a spherical volume of uniform internal and negligible external density and magnetic fields, the ratio between gravitational (W) and magnetic (E_m) energies is given by

$$\frac{|W|}{E_m} = \frac{C_m G M^2 R^{-1}}{(1/8\pi)\int_V B^2 dV}, \tag{1.1}$$

where C_m is a constant that depends on the mass distribution and geometry, for the case of spherical geometry C_m=3/5, G is the gravitational constant, M is the mass contained in the volume, R is the radius of the volume, V is integration volume, and B is the magnetic field strength. The denominator of equation (1.1) can be written in terms of the magnetic flux through a cross-sectional area A of the volume V perpendicular to $\vec{B}$,

$$\Phi = \int_A \vec{B} \cdot \hat{n}\, dA \approx \pi R^2 B, \tag{1.2}$$

where $\hat{n}$ is the unit vector perpendicular to the area A, and the second equality holds approximately under the assumption of a spherical region of radius R with a uniform magnetic field, for which, in addition,

$$\int_V B^2 dV \approx \frac{4\pi B^2 R^3}{3}. \tag{1.3}$$

So, from equations (1.2) and (1.3), equation (1.1) can be written as:

$$\frac{|W|}{E_m} = \frac{6 C_m \pi^2 G M^2}{\Phi^2}. \tag{1.4}$$

When this energy ratio is equal to one, the cloud is in equilibrium between gravity and the magnetic pressure gradient. This allows us to define a critical mass-to-flux ratio,

$$\left(\frac{M}{\Phi}\right)_{crit} = \frac{1}{\sqrt{6 C_m \pi^2 G}}. \tag{1.5}$$

Equation (1.5) is used as a normalization constant to obtain the dimensionless mass-to-flux ratio:

$$\mu \equiv \left(\frac{M}{\Phi}\right) / \left(\frac{M}{\Phi}\right)_{crit}. \tag{1.6}$$

The dimensionless mass-to-flux ratio (from now on, mass-to-flux ratio or μ) is used to classify molecular clouds as *sub-critical* if $\mu < 1$ when they are magnetically supported, or *super-critical* if $\mu > 1$ when they are not (Mestel & Spitzer, 1956).

A relevant feature of the mass-to-flux ratio is that it does not depend on the cloud size as long as it conserves its mass. In other words, if we consider a Lagrangian volume enclosing the molecular cloud that is initially sub-critical ($\mu < 1$) and ideal MHD, no compression can make the gravitational energy greater than magnetic energy, which would produce a collapse.

Another relevant aspect of the mass-to-flux ratio is the model used to define it. As mentioned earlier, it assumes negligible external mass, thus the molecular cloud is isolated and does not accrete mass from surrounding regions.

In ideal MHD, the magnetic flux is conserved because in this regime the fluid is a perfect conductor. In other words, the electric resistivity is zero and diffusion does not affect the evolution of the magnetic field. Therefore considering the isolated cloud assumption, the mass-to-flux ratio does not evolve in ideal MHD according to the standard magnetic support model. The only possible way this quantity can evolve for a molecular cloud with constant mass is by considering diffusive processes which break the ideal MHD regime.

The standard magnetic support model considers that ambipolar diffusion is the most common diffusive process responsible for the evolution of the mass-to-flux ratio. Ambipolar diffusion consists of the separation of the neutral and ionized gas (Mestel & Spitzer, 1956), so the neutral gas regions lose magnetic support, become super-critical, and collapse as a consequence (Shu, 1992). More recently, Lazarian et al. (2012) proposed magnetic reconnection as another magnetic diffusion mechanism.

In most numerical simulations, even those considering the ideal MHD regime, there is numerical diffusion of the magnetic field due to the discretization applied in the solution of the fluid equations. This kind of diffusion can also result in the loss of magnetic support. In Section 2.1.1, we explain how numerical diffusion of the magnetic field changes the relevant equation for the evolution of magnetic fields, and in Chapter 3, we propose a resolution criterion to resolve magnetic fields in simulations of molecular clouds that helps to deal with numerical magnetic diffusion.

1.3.2. Turbulent Support Model

The turbulent support model assumes that magnetic fields are not important and that the supersonic turbulent pressure is the main support mechanism against gravitational collapse (e.g., Elmegreen, 2000; Mac Low & Klessen, 2004).

This model arises as an interpretation of supersonic line widths in molecular clouds (Wilson et al., 1970), which were thought to arise from small scale turbulence that can provide a roughly isotropic pressure gradient capable of providing support against gravitational collapse (Zuckerman & Evans, 1974).

The turbulent support model arises from the observed nearly equipartition between the non-thermal kinetic and the gravitational energies (Larson, 1981; Heyer et al., 2009), which is

interpreted as evidence of virial equilibrium between turbulence and gravity. However, this can also be evidence of collapse since virial and free-fall velocities have similar magnitudes (Ballesteros-Paredes et al., 2011). Also, it must be considered that numerical and analytical studies have shown that hydrodynamic and magnetohydrodynamic turbulence dissipate too fast to provide the necessary support (e.g. Mac Low et al., 1998; Ostriker et al., 1999b; Padoan & Nordlund, 1999; Avila-Reese & Vázquez-Semadeni, 2001), which made it necessary to have continuous injection turbulent sources (Vazquez-Semadeni et al., 2000; Mac Low & Klessen, 2004), while stellar feedback is an episodic energy injection mechanism.

1.4. Global Hierarchical Collapse Model

In contrast to the model described in the previous section, the global hierarchical collapse model is not a quasi-stationary model for cloud evolution, and it considers collapses within collapses in which structures accrete mass from their parent structures (Vázquez-Semadeni et al., 2019). According to this model, small-scale dense regions collapse later than their parent structures because they first need to become gravitationally unstable themselves. However, when this happens, they collapse faster due to their shorter free-fall time.

The global hierarchical collapse model also arises from the observation of supersonic line widths in molecular clouds (Wilson et al., 1970) because they were initially interpreted as evidence of gravitational collapse by Goldreich & Kwan (1974). However, this claim was rejected by Zuckerman & Palmer (1974) and Zuckerman & Evans (1974) for two reasons. First, such a gravitational collapse would result in a star formation rate two orders of magnitude greater than the observed one. Second, a systematic shift between absorption and emission lines coming from the external and internal regions of the cloud, respectively, was not observed.

1.5. Magnetic Field Alignment with Cold Atomic Clouds

In addition to the support against gravitational collapse provided by the Lorentz force, a tight correlation between the orientation of the magnetic field and CACs has been identified in the last decade. For example, Clark et al. (2015) nd Planck Collaboration et al. (2016a) found that the plane of the sky magnetic field, detected using polarized thermal dust emission, is aligned with atomic hydrogen structures detected with HI emission and molecular structures traced by dust respectively. Clark et al. (2014) also observed this alignment in HI fibers, which are thin long dense structures detected in HI emission using the Rolling Hough transform with column densities $N \approx 10^{-19}$ cm^{-2}, volume densities $n \approx 14$ cm^{-3}, and temperatures $T < 220$ K. An example is shown in Figure 1.1, where HI Fibers detected at the Riegel-Crutcher cloud look in alignment with polarization pseudo vectors. In addition, Planck Collaboration et al. (2016b) found that the relative orientation of the projected magnetic field and dust filaments changes from parallel to perpendicular when sampling higher density regions in nearby MCs.

However, the correlation's precise role and importance remain unclear, as most of the observational evidence refers to spatial and orientation correlations without a clear understanding of the causality involved. Therefore, it is crucial to understand the interplay between the molecular clouds' (MCs) precursors and magnetic fields. CACs are thought to constitute the primordial place for earlier stages of the evolution of molecular clouds

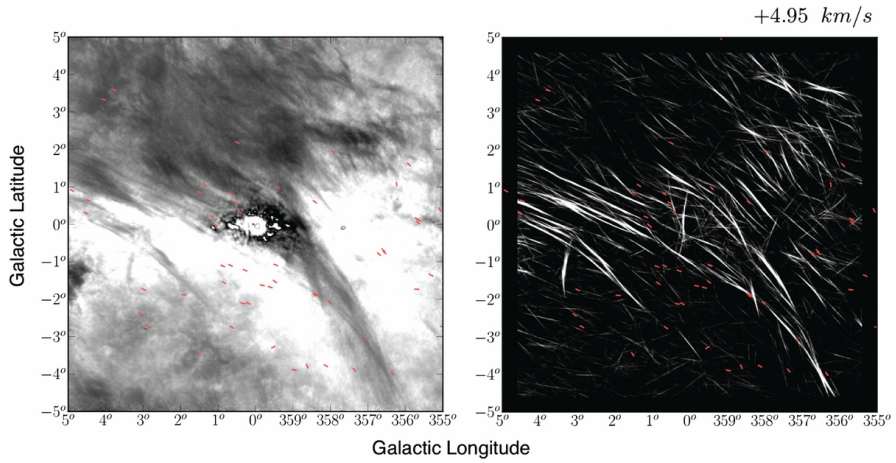

Figure 1.1: Left: The Riegel-Crutcher cloud with polarization pseudovectors in red representing polarization angles from Heiles (2000). Right: Fibers obtained in this cloud with the Rolling Hough transform and superposed with the pseudovectors. Note the alignment between the fibers and polarization pseudo vectors. Reproduced from Clark et al. (2014)

and, eventually, star formation (e.g., Koyama & Inutsuka, 2002; Audit & Hennebelle, 2005; Vázquez-Semadeni et al., 2006; Heitsch et al., 2006); therefore, understanding the alignment mechanism of magnetic field lines in CACs is relevant to elucidate the role of magnetic fields.

Hennebelle (2013) studied the formation of non-self-gravitating CACs in the ISM. This author focused on finding the mechanism responsible for the elongation of CACs and concluded that the clouds are generated by the stretching induced by turbulence because they are aligned with the strain. Moreover, the author also found that the Lorentz force confines CACs.

Soler et al. (2013) proposed a statistical tool to measure the angle between the magnetic field and the density gradient of structures in the ISM which they referred to as the histogram of relative orientations (HRO), which is based on the histogram of oriented gradients (Leonardis et al., 2006). Using synthetic observations of MHD, gravitational, and isothermal simulations of molecular clouds, the authors found that the relative orientation of the magnetic field and isodensity contours either changes from parallel to perpendicular, parallel to non-preferred, or stays parallel, for a high, medium, and low magnetization, respectively. An example of the HRO diagram is shown in Figure 1.2, where it was applied to the IC 5146 region (Planck Collaboration et al., 2016b) and shows that the angle between the magnetic field and the density contours (ϕ[1]) changes from parallel to perpendicular when the column density interval increases.

In Figure 1.3, we show a sketch of a density contour and a magnetic field to clarify what is the angle (ϕ) . In this Figure, the left panel represents the case when the density gradient is perpendicular to the magnetic field, which means $\phi = 90°$ or $\cos\phi = 0$, so that the magnetic field is parallel to the density contour. The other case on the right panel happens when the density gradient and the magnetic field form $\phi = 0°$ or $\cos\phi = 1$, which corresponds to the magnetic field being perpendicular to the density isocontours.

[1]Note that this angle definition differs from the one applied in Soler et al. (2013) and Soler & Hennebelle (2017), in which ϕ is the angle between the magnetic field and the density gradient. In this work, we prefer to use this definition to compare with the results reported in those publications.

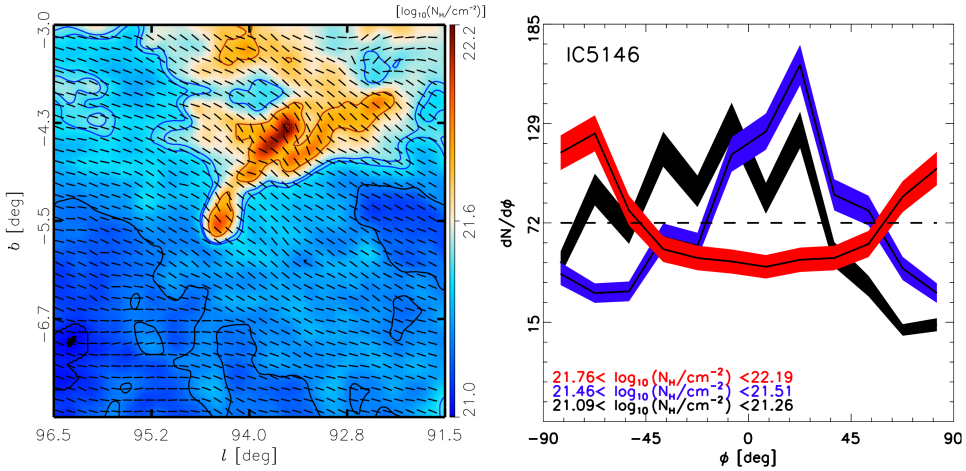

Figure 1.2: Left: column density maps and magnetic field pseudo-vectors. This region corresponds to the molecular cloud complex IC 5146 in Cygnus located at $d \approx 400$ pc. Right: The obtained HRO for this region. Note that the alignment between density structures and the local magnetic field changes from parallel to perpendicular when increased the sampled density. Reproduced from Planck Collaboration et al. (2016b).

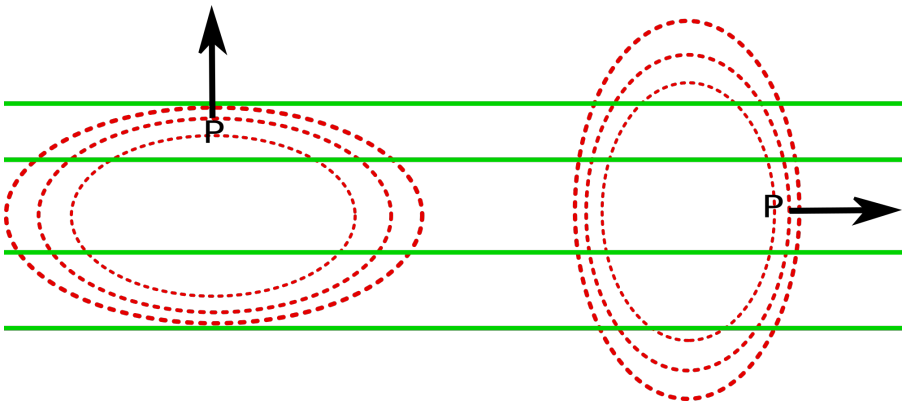

Figure 1.3: Alignment between the density gradient and the magnetic field. The dashed red lines represent the density isocontours while the black and green arrows are the density isocontours gradients and the magnetic field respectively. In the left panel, the magnetic field is parallel to the isocontour and perpendicular to the density gradient ($\phi = 90°$) and in the right panel the magnetic field is perpendicular to the isocontour and parallel to the density gradient ($\phi = 0°$) on the positions shown by the black arrow (P).

More recently, Soler & Hennebelle (2017) studied the evolution of the angle between density gradients and magnetic field (ϕ) with an analytic approach based on the transport equations of MHD turbulence. They found that ϕ values that correspond to the density gradients being parallel ($\phi = 0°$) or anti-parallel ($\phi = 180°$) and perpendicular ($\phi = 90°$) to the magnetic field are equilibrium points. Therefore, they argue, the system tends to evolve to these ϕ values that correspond to the magnetic field being perpendicular and parallel to the density contours.

In addition, Inoue & Inutsuka (2016) studied the origin of the magnetic field alignment with fibers in simulations of HI clouds formed in a shock-compressed layer resembling the local bubble. They found that the origin of the formation of fibers and their alignment with magnetic fields is the turbulent shear strain, which is also the reason for the elongation of filamentary CACs found by Hennebelle (2013).

One important fact related to the alignment of CACs with the magnetic field is the expectation that CACs accrete mass along the magnetic field lines (e.g., Hartmann et al., 2001; Vázquez-Semadeni et al., 2011). This arises due to the findings of Field (1965) about TI, more precisely, the fact that for the magnetic TI, condensations can grow unaffected by the Lorentz force along the magnetic field direction, but they can be suppressed in the direction perpendicular to the magnetic field. However, for typical conditions of the WNM ($n \sim 1\,\mathrm{cm}^{-3}$, $T \sim 5000\mathrm{K}$, $\sigma_v \sim 10\,\mathrm{km\,s}^{-1}$, $B \sim 3\,\mu\mathrm{G}$), we could have instead super-Alvénic motions, for which the magnetic field lines do not dominate the accretion of gas, but rather are dragged by the flow.

In Chapter 4, we study the alignment of the magnetic field with CACs tracking the evolution of magnetic field lines. The results from studying this research topic will be submitted shortly as the second publication of the Ph.D. program.

2

Physical Background

In this chapter, we describe the relevant physics for the formation of clouds in the ISM and the alignment of CACs with the magnetic field. A qualitative description of these processes can be found in Chapter 1.

2.1. Magnetohydrodynamic Equations

As mentioned in Section 1.1, the ISM is described by the equations of fluid dynamics. These equations express mass, momentum, and energy conservation. When considering the effects of gravity, cooling and heating mechanisms, and magnetic fields, these equations are:

$$\frac{\partial \rho}{\partial t} + \boldsymbol{u} \cdot \nabla \rho = -\rho \nabla \cdot \boldsymbol{u}, \tag{2.1}$$

the mass conservation equation,

$$\frac{\partial \boldsymbol{u}}{\partial t} + \boldsymbol{u} \cdot \nabla \boldsymbol{u} = -\frac{\nabla P}{\rho} - \nabla U + \frac{1}{4\pi\rho}(\nabla \times \boldsymbol{B}) \times \boldsymbol{B}, \tag{2.2}$$

the momentum conservation equation, and

$$\frac{\partial e}{\partial t} + \boldsymbol{u} \cdot \nabla e = -(\gamma - 1) e \nabla \cdot \boldsymbol{u} + \Gamma - n\Lambda, \tag{2.3}$$

the energy conservation equation. In these equations, ρ, $\boldsymbol{u}$, P,U, $\boldsymbol{B}$, e, γ, Γ, and $n\Lambda$ are the mass density, velocity vector, thermal pressure, gravitational potential, magnetic field, internal energy per unit volume, the ratio of specific heats, rate of heating, and rate of cooling. The rates of radiative heating (Γ) and cooling ($n\Lambda$) incorporate all the heating and cooling physical mechanisms relevant to the ISM (See Section 1.1).

Equations (2.1), (2.2), and (2.3) are also known as the mass, momentum, and energy conservation equations respectively, and they have the same shape. On the left-hand side, there is the temporal rate of change of the physical quantity Q and the transport of the spatial variation of the same quantity $\boldsymbol{u} \cdot \nabla Q$, and on the right hand of the equality the source terms for Q.

For the mass conservation equation (2.1), the source term is $-\rho \nabla \cdot \boldsymbol{u}$, which means that to increase the density, the gas should converge to the region, or equivalently, have a negative

velocity divergence. In the momentum conservation equation (2.2), the source terms are the negative of the pressure gradient per density, which means that the fluid moves from high to low pressures, the negative of the gravitational potential, meaning that the gas moves from regions of higher to lower gravitational potential values, and the Lorentz force which may be written as the sum of a magnetic pressure gradient and a magnetic tension:

$$\boldsymbol{F}_L = \frac{1}{4\pi}(\nabla \times \boldsymbol{B}) \times \boldsymbol{B} = -\frac{1}{8\pi}\nabla B^2 + \frac{1}{4\pi}(\boldsymbol{B} \cdot \nabla)\boldsymbol{B}. \tag{2.4}$$

The first term on the right hand side of equation (2.4) is the gradient of the magnetic pressure, $B^2/8\pi$, and the second one is often called magnetic tension or the magnetic curvature force and it describes a force due to the variation of the magnetic field strength in the direction of the magnetic field.

The source terms for the energy conservation equation (2.3) are the adiabatic work (PdV; first term) done on the fluid parcel and the cooling and heating processes that change its internal energy.

In addition to the Euler equations, MHD considers the induction or flux freezing equation,

$$\frac{\partial \boldsymbol{B}}{\partial t} = \nabla \times (\boldsymbol{u} \times \boldsymbol{B}), \tag{2.5}$$

which describes the evolution of the magnetic field in the ideal MHD regime in which the fluid is a perfect conductor; in other words, in the absence of electrical resistance (infinite conductivity).

In addition to the fluid equations, the dynamics of self-gravitating fluids must also follow the Poisson equation, which describes how the gravitational potential changes in different regions due to the mass spatial distribution:

$$\nabla^2 U = 4\pi G\rho, \tag{2.6}$$

where G is the gravitational constant. Furthermore, it is also necessary to have a relation between the pressure P and the internal energy per unit volume e given by the equation of state,

$$P = \rho(\gamma - 1)e. \tag{2.7}$$

Numerical simulations can solve the equations of fluids using numerical techniques such as grid-based or smoothed particle hydrodynamics. Grid-based hydrodynamics discretizes these equations obtaining a system of finite difference equations, while smoothed particle methods are an extension of the N-body particle method that includes the properties of gases. In numerical solutions obtained with these methods, there is numerical diffusion of the physical variables due to the approximations made. In the case of the magnetic field, this diffusive effect leads to the departure of the gas from the perfect electrical conductivity assumption.

2.1.1. Magnetic Diffusion

When ideal MHD is not valid the electric conductivity is not infinite anymore, and it is necessary to include a diffusive term on the right side of equation (2.5). This diffusive term includes the electric resistivity or magnetic diffusion coefficient η, where

$$\eta = \frac{c^2}{4\pi\sigma_e}, \tag{2.8}$$

where c is the speed of light and σ_e is the electric conductivity. When including this term, equation (2.5) is written instead as (Bodenheimer, 2007)

$$\frac{\partial \boldsymbol{B}}{\partial t} + \nabla \times (\boldsymbol{B} \times \boldsymbol{u}) = -\nabla \times (\eta \nabla \times \boldsymbol{B}). \tag{2.9}$$

In the case when the magnetic diffusion is not physical but numerical instead, its effect on the magnetic field may still be described by the equation (2.9).

2.1.2. Numerical Magnetic Diffusion and Resolution Criteria

As mentioned in Section 1.3.1, two possible physical mechanisms that can produce magnetic diffusion are ambipolar diffusion and magnetic reconnection. However, simulations not considering these diffusive processes, i.e., under the ideal MHD regime, can also have numerical magnetic diffusion instead.

When the magnetic field is insufficiently resolved, a simulation that is in principle sub-critical ($\mu < 1$), i.e., supported by the magnetic field against gravitational collapse (See section 1.3.1) may nevertheless undergo spurious gravitational collapse due to numerical diffusion of the magnetic flux.

Resolution criteria are necessary for the adequate numerical simulation of every physical process. For example, Truelove et al. (1997) found that resolving the Jean's length with a minimum of four cells avoids spurious fragmentation on AMR hydrodynamic simulations of isothermal molecular clouds. Furthermore, Bate & Burkert (1997) found a similar resolution condition for SPH simulations. Also, Koyama & Inutsuka (2004) found that at least three cells are necessary to resolve the Field length and to achieve convergence of some properties such as the number of clouds formed by thermal instability and the maximum Mach number in simulations of the development of turbulent motions driven by the non-linear evolution of thermal instability. More recently, Federrath et al. (2011) studied the gravity-turbulence-driven magnetic field amplification of super-critical clouds. They found that it is necessary to resolve the Jeans length with at least 30 cells to resolve turbulence at the Jeans scale and capture minimum dynamo amplification of the magnetic field.

Resolution criteria are usually obtained through convergence tests, which consist of increasing the resolution until a certain feature of the flow remains invariant. In this sense, convergence tests constitute a trial-and-error procedure. In Chapter 3, we propose a resolution criterion based on measuring a "numerical diffusion coefficient" via a test problem instead. Once this coefficient is known, the dependence of the numerical diffusion timescale on the resolution can be inferred and compared with the characteristic timescale of the physical process of interest. Specifically, the requirement of our resolution criterion is that the diffusion time needs to be longer than the relevant dynamical time of the structure. Thus, this procedure provides a physically-motivated prescription for the necessary numerical resolution. In Chapter 3, we present an application to the problem of adequately resolving the magnetic support against the self-gravity of a dense molecular cloud. These results were published in MNRAS (Granda-Muñoz et al., 2022).

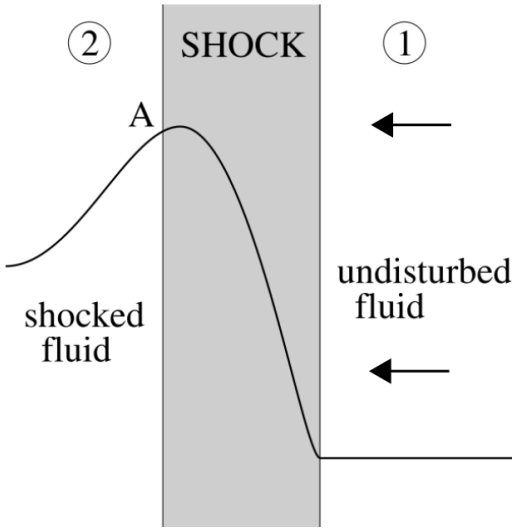

Figure 2.1: Shock front representation. The region denoted by 1 represents the unshocked or the undisturbed region, the one represented by 2 is the shocked or the disturbed region, and the density profile is represented by the solid dark line. The figure is shown in the shock rest frame and the fluid moves from right to left in this frame. Reproduced from Boyd & Sanderson (2003).

2.2. Shocks

An important physical process in the supersonic turbulent ISM is the formation of shocks. Shocks play a crucial role in the energy balance of the present phases in the ISM because they convert kinetic to thermal energy. For example, shocks generated by supernova explosions yield the hot, low-density third phase of the ISM (McKee & Ostriker, 1977).

In the Earth, the most famous evidence of shocks is given by the passage of supersonic planes that creates a sonic boom. So, the generation of shocks is related to matter moving supersonically. The reason is that when matter travels at a velocity larger than the sound speed, it moves faster than the velocity at which the information propagates; in other words, the sound speed. In this scenario, a shock generates a change in the shocked medium that happens faster than its reaction time. That is why, the pre-shock region has not time to react to the approaching shock, which yields sudden changes in the physical properties in a region called the shock front. Figure 2.1 shows a representation of a shock front, where region 1 is the unshocked fluid also called the upstream region, and region 2 is the shocked or downstream region.

The study of shocks can be done analytically with a set of equations called the *jump conditions*, which relate to how the physical properties of the fluid change before and after the shock front. To obtain them, it is convenient to use a reference frame where the shock is at rest and the flow is stationary, which means that all variables are time-independent. In addition, the shock front thickness is of the order of the particle mean free path $\tilde{\lambda}$; therefore, it can be approximated as a plane with an infinitesimal thickness if $\tilde{\lambda}$ is much smaller than the dimensions of the system in question. For the ideal MHD regime, the jump conditions are obtained from the MHD fluid equations (see Section 2.1) and are usually called the Rankine-Hugoniot equations. Restricting for simplicity to plane shocks that move in the direction normal to the shock front (x direction), the jump conditions are usually represented by the

operator $[a]_1^2 = a_2 - a_1$, where a is a physical quantity, and the subscripts 1 and 2 represent the upstream or the pre-shock and the downstream or post-shock regions, respectively.

The jump conditions result from the conservation of physical quantities, and they are found from the integral form of the fluid equations across the shock. After doing that, we get

$$[\rho \boldsymbol{u} \cdot \hat{s}]_1^2 = 0, \tag{2.10}$$

$$\left[\rho \boldsymbol{u}(\boldsymbol{u} \cdot \hat{s}) + \left(P + \frac{B^2}{8\pi}\right)\hat{s} - (\boldsymbol{B} \cdot \hat{s})\frac{\boldsymbol{B}}{4\pi}\right]_1^2 = 0, \tag{2.11}$$

$$\left[\boldsymbol{u} \cdot \hat{s}\left\{\left(\rho I + \frac{\rho u^2}{2} + \frac{B^2}{8\pi}\right) + \left(P + \frac{B^2}{8\pi}\right)\right\} - \frac{(\boldsymbol{B} \cdot \hat{s})(\boldsymbol{B} \cdot \boldsymbol{u})}{4\pi}\right]_1^2 = 0, \tag{2.12}$$

$$[\boldsymbol{B} \cdot \hat{s}]_1^2 = 0, \tag{2.13}$$

and

$$[\hat{s} \times (\boldsymbol{u} \times \boldsymbol{B})]_1^2 = 0, \tag{2.14}$$

where

$$I = \frac{P}{(\gamma - 1)\rho}. \tag{2.15}$$

Equations (2.10), (2.11), and (2.12) result from the mass, momentum, and energy conservation. The last two equations (2.13) and (2.14) constitute the jump conditions for the perpendicular and tangential magnetic field components, where equation (2.13) comes from integrating the equation $\nabla \cdot \boldsymbol{B} = 0$, and equation (2.14) comes from the integration of the induction equation (equation (2.5)) in steady state.

From the jump condition equations, it is possible to know how physical variables change after the shock front and study different kinds of shocks. One way to classify shocks relies on the angle (θ) between the unshocked or the upstream magnetic field, $\boldsymbol{B}_1$, and the normal to the shock front, $\hat{s}$. In this way, shocks are classified as parallel ($\theta = 0$), perpendicular ($\theta = \pi/2$) and oblique ($0 < \theta < \pi/2$).

2.2.1. Parallel Shocks

For this kind of shock, both $\boldsymbol{u}_1$ and $\boldsymbol{B}_1$ are parallel to $\hat{s}$, i.e., the upstream magnetic and velocity fields are completely perpendicular to the shock front. Therefore from equation (2.13) it is obtained that $\boldsymbol{B}_2 = \boldsymbol{B}_1$ and from equation (2.14) we can also get that $\boldsymbol{u}_2$ is also parallel to $\hat{s}$. These results allow us to cancel out the magnetic field from the jump conditions and obtain,

$$\rho_1 u_1 = \rho_2 u_2, \tag{2.16}$$

$$\rho_1 u_1^2 + P_1 = \rho_2 u_2^2 + P_2, \tag{2.17}$$

and

$$\rho_1 u_1 I_1 + P_1 u_1 + \rho_1 u_1^3/2 = \rho_2 u_2 I_2 + P_2 u_2 + \rho_2 u_2^3/2, \tag{2.18}$$

where equation (2.18) can be rewritten using equations (2.15) and (2.16) as

$$\frac{\gamma P_1}{(\gamma - 1)\rho_1} + \frac{u_1^2}{2} = \frac{\gamma P_2}{(\gamma - 1)\rho_2} + \frac{u_2^2}{2}. \tag{2.19}$$

Therefore, the jump conditions for the parallel shock are equivalent to the case of a hydrodynamic shock.

2.2.2. Perpendicular Shocks

For this kind of shock, the upstream magnetic field is perpendicular to $\hat{n}$ or parallel to the shock front plane. From equation (2.13), we know that the magnetic field at the post-shock region also needs to be perpendicular to $\hat{n}$. Furthermore, from equation (2.10), we obtain

$$\boldsymbol{u}_2 = \frac{\rho_1}{\rho_2}\boldsymbol{u}_1. \tag{2.20}$$

The post-shock magnetic field is found from equation (2.14)

$$\boldsymbol{B}_2 = \frac{\rho_2}{\rho_1}\boldsymbol{B}_1, \tag{2.21}$$

thus, the magnetic field remains parallel to the shock front but it increases its magnitude by the same factor the gas density increases. It can also be shown that in order to form perpendicular shocks, it is necessary to have $u_1^2 > c_s^2 + u_{\mathrm{A}}^2$, where $u_{\mathrm{A}} = B/\sqrt{4\pi\rho}$ is the Alfvén speed.

2.2.3. Oblique Shocks

For this kind of shock, $\boldsymbol{u}$ and $\boldsymbol{B}$ have components both parallel and perpendicular to the shock front. Therefore, it is convenient to choose a frame of reference known as the *Hoffmann-Teller frame* where $\boldsymbol{u}_1 \times \boldsymbol{B}_1 = 0$, i.e.; a reference frame moving at the velocity in which $\boldsymbol{u}_1 \parallel \boldsymbol{B}_1$, this means

$$u_{1y} = u_{1x}B_{1y}/B_x, \tag{2.22}$$

where $B_x = B_{1x} = B_{2x}$.

In addition from equation (2.14), we obtain

$$u_{2y} = u_{2x}B_{2y}/B_x, \tag{2.23}$$

thus, from equations (2.22) and (2.23) we can obtain:

$$\frac{u_{2y}}{u_{1y}} - 1 = \frac{B_x B_{1y}}{4\pi\rho_1 u_{1x}u_{1y}}\Big(\frac{B_{2y}}{B_{1y}} - 1\Big) = \frac{B_1^2}{4\pi\rho_1 u_1^2}\Big(\frac{B_{2y}}{B_{1y}} - 1\Big), \tag{2.24}$$

which, combined with equation (2.23), gives

$$\frac{u_{2y}}{u_{1y}} = \frac{u_1^2 - u_{\mathrm{A}}^2}{u_1^2 - r_\rho u_{\mathrm{A}}^2} = \frac{B_{2y}}{r_\rho B_{1y}}, \tag{2.25}$$

where $r_\rho = \rho_2/\rho_1$. The relation between upstream and downstream magnetic fields given by equation (2.25) can be written differently when the frame of reference is one in which $u_1 = u_{1x}$, in this case, we have that

$$\frac{B_{2y}}{r_\rho B_{1y}} = \frac{u_1^2 - u_{\mathrm{A}}^2\cos\theta^2}{u_1^2 - r_\rho u_{\mathrm{A}}^2\cos\theta^2}, \tag{2.26}$$

where θ is the angle between the upstream magnetic field B_1, and the normal to the shock front $\hat{n}$. It is clear from equation (2.25) that $B_{2y} > B_{1y}$ when $u_1^2 \geq r_\rho u_{\mathrm{A}}^2 > u_{\mathrm{A}}^2$ and $B_{2y} < B_{1y}$

when $u_1^2 \leq u_A^2 < r_\rho u_A^2$. The first case is called a fast shock while the second one is a slow shock. They are both represented in Figure 2.2, where we can see at the top left panel that the parallel component to the shock front of the magnetic field is amplified for a fast shock while at the top right panel the parallel component of the magnetic field is reduced.

The fast and slow shocks have two special limiting cases. First, when $u_1^2 = r_\rho u_A^2$ from equation (2.25) we obtain that $B_{1y} = 0$ for the fast shock. In this case, the fast MHD shock is called switch-on because it generates a magnetic field component parallel to the shock front plane (perpendicular to $\hat{n}$). Second, when $u_1^2 = u_A^2$, from equation (2.25), we have $B_{2y} = 0$. Therefore, this slow shock is called a switch-off because it eliminates the magnetic field component parallel to the shock front plane (See bottom panels of Figure 2.2).

Oblique shocks, in particular fast oblique shocks, are important to yield the observed alignment of magnetic field lines with cold atomic clumps because of the amplification of the magnetic field component parallel to the shock front (See Chapter 4).

2.3. Relevant Instabilities for Cloud Formation

A physical system described by nonlinear equations is prone to instabilities (Faber, 1995). One example of such a system is the ISM, which is described by the MHD equations as mentioned in Section 2.1. Therefore, instabilities are inherent to the ISM.

The development of instabilities in physical systems is related to their equilibrium. The equilibrium of a physical system may be classified as stable or unstable. It is stable when the perturbed physical variables oscillate around their initial unperturbed state. In contrast, it is unstable when the perturbation causes the exponential growth of its physical variables. Linear perturbation theory is applied to the study of stability in physical systems. It consists of introducing perturbations in the system at a given configuration that might trigger the instability and checking if these perturbations grow or oscillate with time.

In this section, we do not describe all the mathematics related to the study of instabilities using linear perturbation theory. We instead show some results and describe the development of the relevant instabilities for cloud formation in the ISM.

2.3.1. The Thermal Instability (TI)

As mentioned in section 1.2, thermal instability is a physical process that triggers the formation of atomic and molecular clouds from the compression of the warm neutral atomic medium and is produced by the multiple cooling and heating processes on the atomic interstellar medium. In this work, we use the cooling and heating functions proposed in Koyama & Inutsuka (2002), [1] which are based on analytic fits to chemical and thermal computations found in Koyama & Inutsuka (2000). The heating function is given by:

$$\Gamma = 2.0 \times 10^{-26} \text{ erg s}^{-1}, \tag{2.27}$$

while the cooling function is:

$$\Lambda = \Gamma\left[10^7 \exp\left(\frac{-1.184 \times 10^5}{T + 1000}\right) + 1.4 \times 10^{-2}\sqrt{T}\exp\left(\frac{-92}{T}\right)\right] \text{ cm}^3, \tag{2.28}$$

[1] With the typographical correction given in Vázquez-Semadeni et al. (2007).

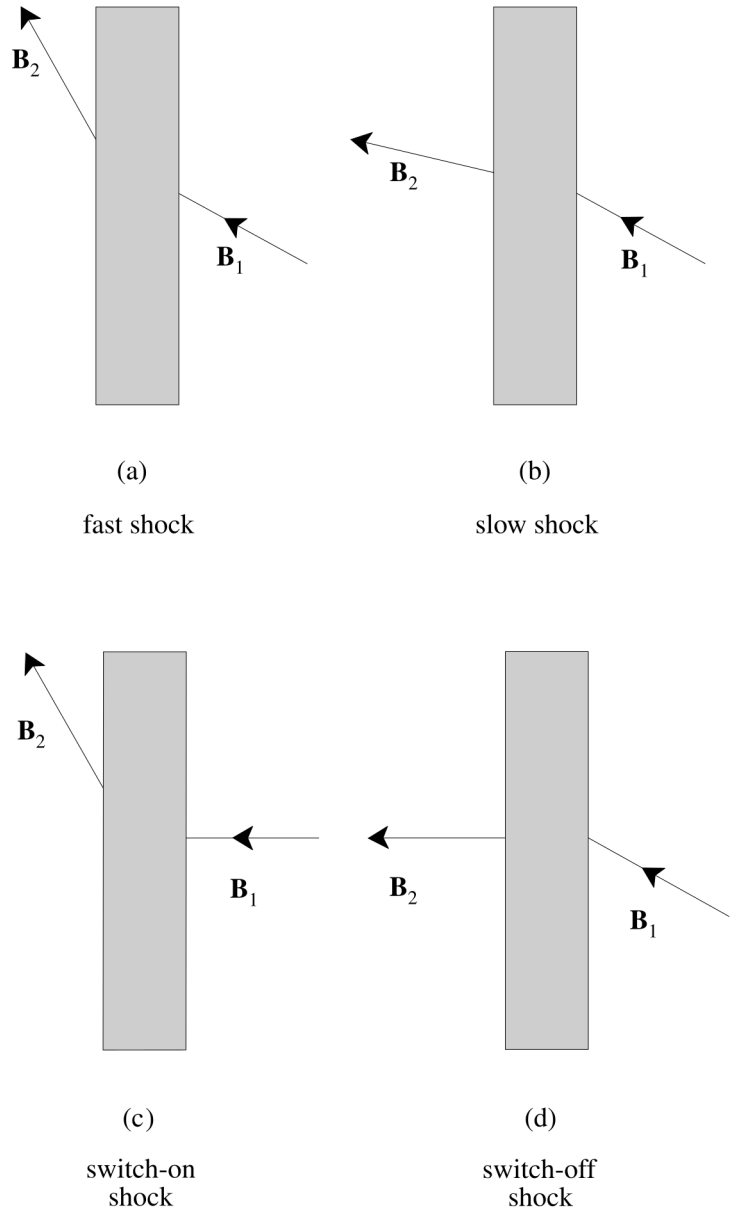

Figure 2.2: Top left: fast shock, top right: slow shock, bottom left: switch-on shock, bottom right: switch-off shock. Reproduced from Boyd & Sanderson (2003)

where T is the temperature. From these functions, the net cooling function is defined as

$$\mathcal{L} = n_H \Lambda(T) - \Gamma, \tag{2.29}$$

where n_H is the atomic hydrogen number density (ρ/m_H).

Thermal equilibrium is achieved when the cooling and heating are equal, i.e., when $\mathcal{L} = 0$. Since this regime is defined by a specific temperature for a given density, it is characterized by the equilibrium pressure shown by the green solid line in Figure 2.3, obtained by substituting the equilibrium density in the ideal-gas equation of state. Above the equilibrium pressure, the rate of cooling is greater than the heating one and $\mathcal{L} > 0$, while bellow the equilibrium curve, the heating rate is greater than the cooling one, so $\mathcal{L} < 0$.

The evolution of a gas parcel initially at thermal equilibrium depends on its position in the equilibrium curve and how it is perturbed away from it. Considering that the initial position of the gas parcel is on any of the two stars shown in Figure 2.3, which correspond to points in regions of stable equilibrium. Considering isobaric perturbations at these points that increase their number density and decrease their temperature (keeping the pressure constant), which are represented by red arrows pointing right at both points, both gas parcels enter the region where the heating is larger than the cooling ($\mathcal{L} < 0$). Therefore, the temperature will increase, causing an expansion and thus a reduction of the parcels' number density leading them to return to their original unperturbed positions, as indicated by the red arrows pointing left. Something similar happens when the perturbation reduces the number density and increases the temperature of both gas parcels (again keeping their pressure constant), which is represented by the blue arrows to the left. In this case, the gas parcels reach the region where the cooling is greater than the heating ($\mathcal{L} > 0$). Therefore, the temperature decreases, the volume decreases, and the number density increases, returning the gas parcels to their original unperturbed position as indicated by the blue arrows to the right.

The evolution of the gas parcel after the isobaric perturbation is different when its initial unperturbed position is in the unstable region of the thermal equilibrium pressure. This initial position is shown by the star in Figure 2.4, and when the perturbation increases its number density and decreases its temperature (blue arrow), the gas parcel enters a region where the cooling is greater than the heating, so its temperature tends to decrease even more and its density increases keeping the isobaric evolution. This process goes on until the gas parcel reaches equilibrium again and becomes part of the cold neutral medium (CNM) which, as mentioned in the former paragraph, is part of the region of stable equilibrium. Therefore, the evolution of the gas parcel stops when it reaches this region.

When the isobaric perturbation decreases the number density and increases its temperature, the gas parcel enters a region where the heating is greater than the cooling (red arrow). Therefore, its temperature increases even more. This process continues isobarically until the gas parcel reaches thermal equilibrium at the phase called the warn neutral medium (WNM), which is also in region of stable equilibrium thus the evolution stops.

Field (1965) studied TI using perturbation theory and found its dispersion relation under the linear regime. This relation gives the dependence of the temporal frequency (ω) with the spatial frequency (k) of the perturbation without considering gravitation and magnetic fields. The dispersion relation is given by:

$$\omega^3 + \omega^2 c\left(\kappa_T + \frac{k^2}{\kappa_K}\right) + \omega c^2 k^2 + \frac{c^3 k^2}{\gamma}\left(\kappa_T - \kappa_\rho + \frac{k^2}{\kappa_K}\right) = 0, \tag{2.30}$$

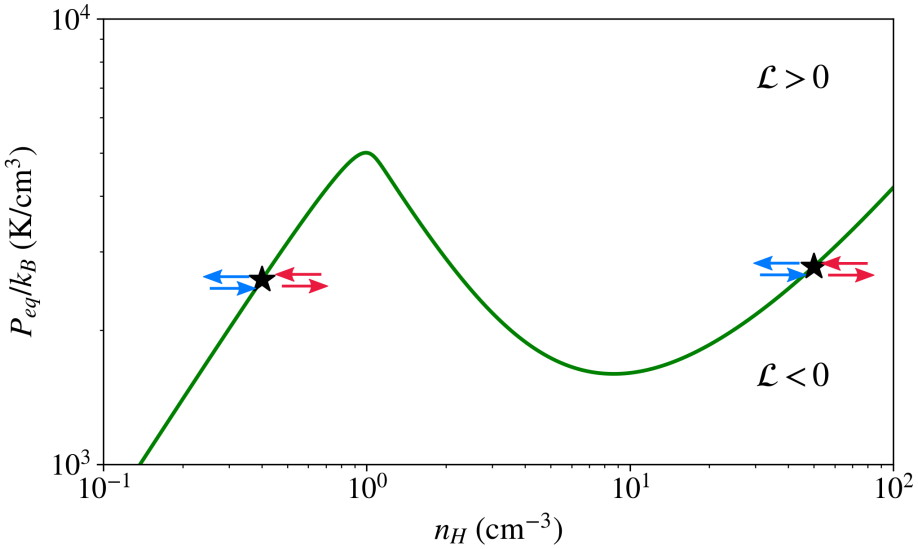

Figure 2.3: Thermal equilibrium pressure vs number density. The equilibrium pressure at a given number density is represented by the green line, and the dark stars represent gas parcels at a stable equilibrium. The red and blue arrows at the gas parcels represent isobaric perturbations leading to the regions where $\mathcal{L} < 0$ and $\mathcal{L} > 0$, respectively.

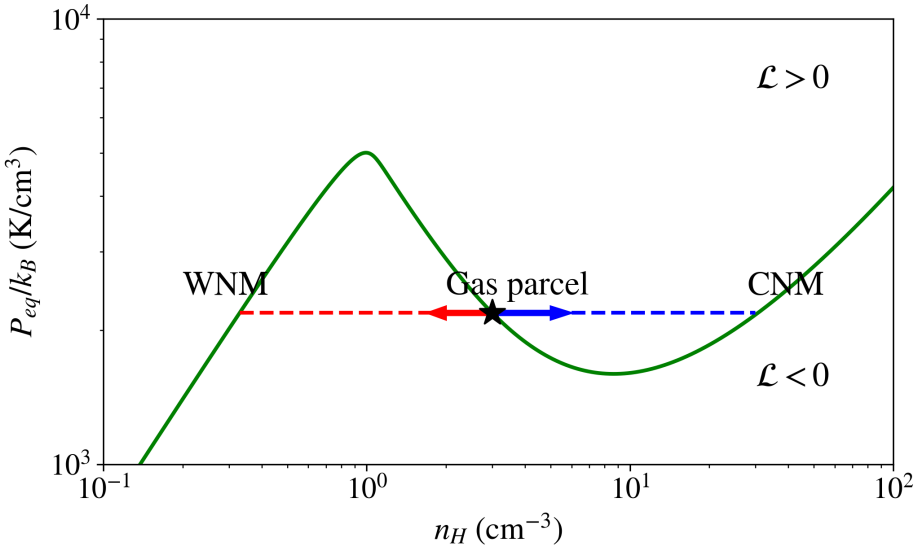

Figure 2.4: Thermal equilibrium pressure vs number density. The equilibrium pressure at a given number density is represented by the green line.

where $c_s = [(\gamma P_0)/\rho_0]^{1/2}$ is the adiabatic sound speed and

$$\kappa_\rho = \frac{\mu\rho_0(\gamma-1)}{RcT_0}\left(\frac{\partial\mathcal{L}}{\partial\rho}\right)_T \ , \kappa_T = \frac{\mu(\gamma-1)}{Rc}\left(\frac{\partial\mathcal{L}}{\partial T}\right)_\rho \ , \kappa_K = \frac{Rc\rho_0}{\tilde{\mu}(\gamma-1)K} \tag{2.31}$$

are the density, temperature, and thermal conductivity wave numbers respectively. Both κ_ρ and κ_T correspond to the wavenumbers of sound waves whose angular frequencies are numerically equal to the growth rate of isothermal and isochoric perturbations, respectively; while κ_K is the wave number corresponding to the mean free path of the conducting particles. R is the ideal gas constant, $\tilde{\mu}$ is the mean molecular weight, ρ_0 is the initial density , T_0 is the initial temperature, and K is the thermal conductivity. Field (1965) solved the dispersion relation (equation (2.30)) for multiple thermal conductivity values finding that larger conductivity values suppress the perturbation growth for large k (small scales) (see Figure 2.5).

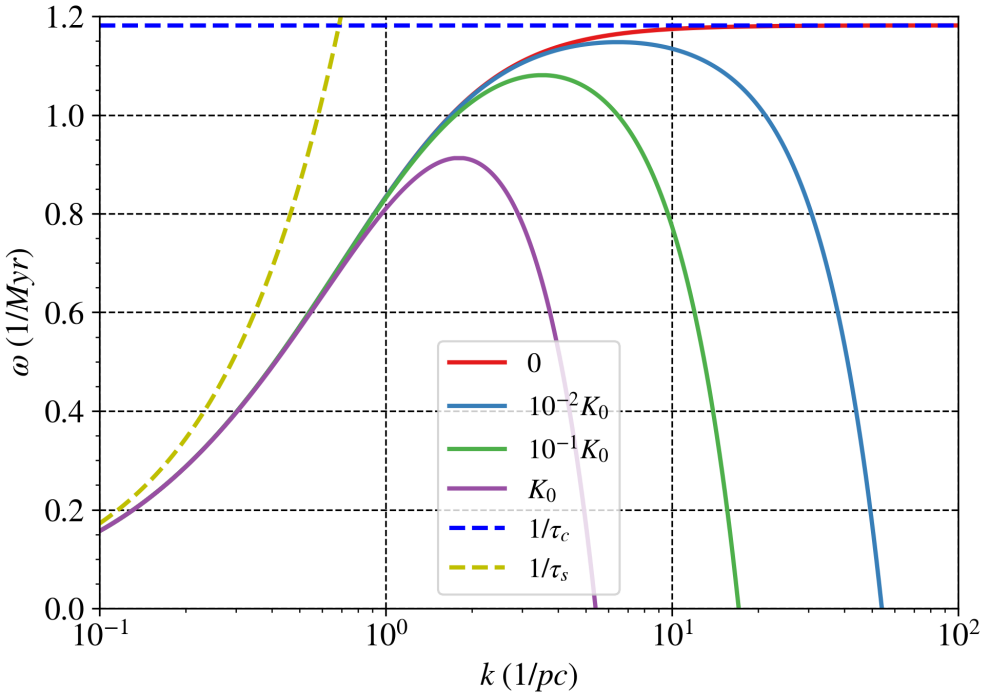

Figure 2.5: Growth rate as a function of the wave number for different values of the thermal conductivity K, which goes from the conductivity parameter K_0 to 0. Notice that larger conductivity values decrease the growth rate for intermediate and large wave numbers and that the growth rate approaches asymptotes given by the inverse of the sound crossing time and the cooling time for short and large wave numbers for the case of zero conductivity, respectively.

From the dispersion relation, it is possible to find two asymptotes that limit the perturbation growth rate as a function of wave number (Field, 1965; Meerson, 1996; Vázquez-Semadeni et al., 2003). For small wave numbers, ω is also small. Thus, taking the limit of equation (2.30)

for ω and k approaching zero, we obtain:

$$\omega_s = \frac{kc}{\sqrt{\gamma}}\left(\frac{\kappa_\rho - \kappa_T}{\kappa_T}\right)^{1/2} \propto \frac{1}{\tau_s}, \tag{2.32}$$

where we have used the notation ω_s to highlight that this time-frequency is proportional to the inverse of the sound crossing time $\tau_s = L/c$. Similarly, the perturbation's growth at large wave numbers (k) and null thermal conductivity (K) can be computed taking the limits of equation (2.30) when k and K approach to infinity and zero respectively:

$$\omega_c = \frac{c}{\gamma}\left(\kappa_\rho - \kappa_T\right) \propto \frac{1}{\tau_c}, \tag{2.33}$$

where ω_c highlights the fact that this asymptote is proportional to the inverse of the cooling time, $\tau_c = 3k_B T/(2|n_H\Lambda - \Gamma|)$.

2.3.2. The Kelvin-Helmholtz Instability (KHI)

The KHI is a fluid instability that happens when there is a velocity shear (i.e., a transverse velocity difference) across the interface between two continuous fluid layers. This instability is visible in a broad variety of places such as in the atmospheres of planets like Jupiter and in cloud formation on Earth.

This instability is named after Lord Kelvin and Hermann von Helmholtz, who were the first known to study it. From there, the linear regime of the KHI has been widely studied. For example, Chandrasekhar (1961) investigated the incompressible hydrodynamic and magnetohydrodynamical cases. For a sharp velocity discontinuity, the growth rate is $k\Delta U$, where $k = \frac{2\pi}{\lambda}$ is the wave number, λ is the wavelength of the perturbation, and ΔU is the velocity at each of the fluid layers (e.g. Heitsch et al., 2006). In other words, a smaller wavelength has higher growth rate than a larger one. Additionally, for the magnetic incompressible KHI, he found that the Lorentz force has a stabilizing effect on the KHI, and the growth rate is $k(\Delta U^2 - u_a^2)^{1/2}$, where u_a is the Alfvén speed.

According to Chandrasekhar (1961), for the non-gravitational case and with a continuous velocity transition between the fluid layers, the KHI instability is unstable when

$$\frac{\tilde{k}}{1 + e^{\tilde{k}}} < 1 < \frac{\tilde{k}}{1 - e^{\tilde{k}}}, \tag{2.34}$$

where $\tilde{k} = 2kd$ is the wave number normalized by the distance between the fluid layers moving at constant speed U, $2d$.

In Figure 2.6, we show a sketch representing how the KHI develops. The region $x_2 > 0$ contains a fluid moving towards the left, while the region $x_2 < 0$ contains a fluid moving to the right. Along the x_1 axis, the black circles at positions na, where $n = 0, \pm1, \pm2, \pm3$, etc, represent the cross-section of vortex lines perpendicular to the plane of the figure, where vortex lines are long straight infinitesimal cylinders that can rotate along their axis. Due to the vorticity generated at the interface between the two regions in Figure 2.6, these vortex lines have the rotation shown in Figure 2.6 by the curvy solid dark vectors around the unperturbed vortex lines. In this unperturbed state, the configuration stays stationary because each vortex cancels out with its neighbors.

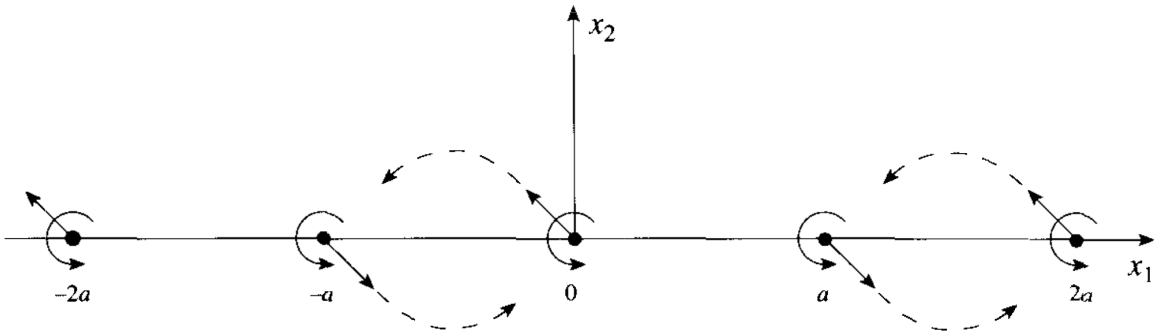

Figure 2.6: Interface between two continuous fluid layers showing vortex lines cross sections located at $x = 0, \pm a, \pm 2a, \pm 3a$, etc. This interface is unstable to small the displacements shown by the solid inclined arrows, and the continuation of these arrows given by the broken curves represent how the vortex lines move and circle around one another after the displacements. Reproduced from Faber (1995).

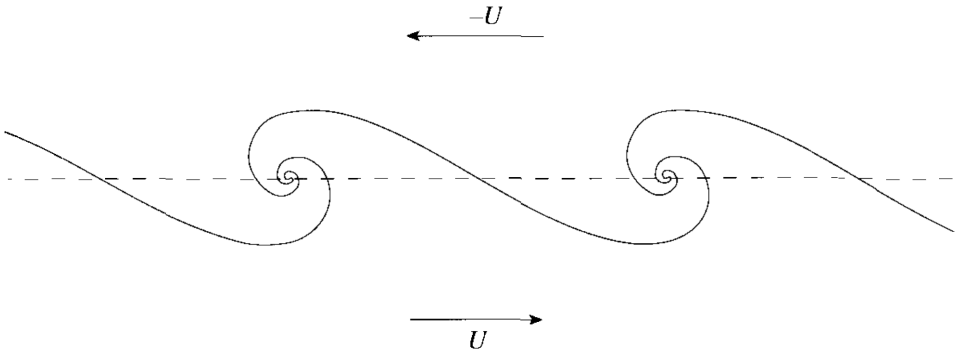

Figure 2.7: Fluid motion after triggering the KHI by the displacement of the interface between the fluids shown in Figure 2.6. Reproduced from Faber (1995)

To understand how the KHI develops, we need to add a perturbation to the described fluid configuration. This perturbation consists in displacing the vortex lines at the interface between the fluid regions moving with different velocities. The displacements along the x_1 and x_2 axis are represented by $\pm\xi_1$ and $\pm\xi_2$, where ξ_1 and ξ_2 are positive. These displacements are of the same magnitude for all vortex lines, but they alternate in sign from one vortex line to the next; for example, for the vortex line located at $x_1 = a$, the displacements are $(\xi_1, -\xi_2)$, while for the vortex line located at $x_1 = 0$, the displacements are $(-\xi_1, \xi_2)$. In Figure 2.6, we can see that these displacements represented by the solid straight black arrows and the subsequent motion of the vortex lines by the broken lines, which means that they pair off with one another producing the flow pattern sketched in Figure 2.7 that constitutes the beginning of the KHI.

2.3.3. The Nonlinear Thin Shell Instability (NTSI)

The nonlinear thin-shell instability arises in a cold slab bounded by two highly supersonic accretion shocks. This instability was initially reported by Hunter et al. (1986), where they studied star formation triggered by high-velocity gas interactions in molecular clouds. Hunter

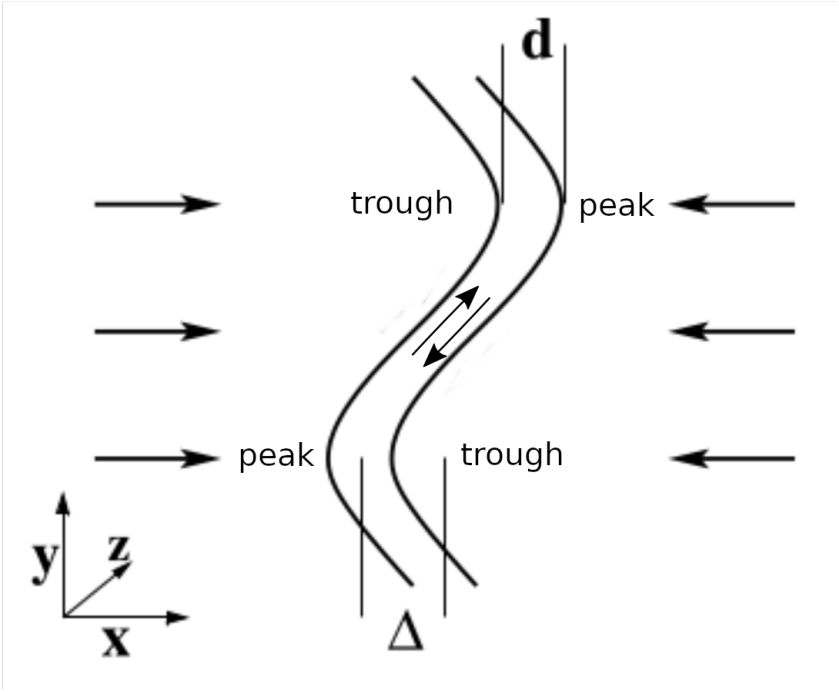

Figure 2.8: The thin shell instability becomes nonlinear when the deviation of the slab (Δ) is comparable to its thickness (d). Note the shear velocity flow in the central part of the slab due to the transfer of longitudinal (along x axis) to transverse momentum (along the y axis). Reproduced from Heitsch et al. (2006)

et al. (1986) reported the presence of a hydrodynamic instability of unknown nature and referred to it as a Rayleigh-Taylor-like instability. A few years later, (Stevens et al., 1992), who studied the collisions of supersonic winds in early binary systems, also reported this instability, and referred to it as a "thin-shell instability".

Vishniac (1994) studied this instability in the linear regime considering the pure hydrodynamic case finding that when the compression ratio of the colliding flows is large (i.e. the square of the Mach number), it can become nonlinear and referred to it as the nonlinear thin-shell instability (NTSI).

The ripples in the slab generated by the colliding flows redirect the incoming shocked gas and produce density enhancements at the troughs of the displaced slab. Specifically, the incoming gas along the x-axis is deflected on the region close to the peaks of the slab and collected at the troughs. In other words, there is a transfer of longitudinal momentum (along the x axis) to lateral momentum (in the y direction). This configuration is shown in Figure 2.8 where d is the slack thickness, and Δ is its displacement. Vishniac (1994) found that when

$$\Delta \geq d, \tag{2.35}$$

i.e., when the perturbation is nonlinear, the system becomes unstable.

An important feature related to the development of this instability is that a shear flow is generated in the region between a peak and a trough, as illustrated in Figure 2.8. This shear can trigger the KHI (see Section 2.3.2). Despite the mathematical complexity of the NTSI, the isothermal case was studied with linear and non-linear perturbation theory. In addition, several numerical studies of the NTSI have been published. Blondin & Marks (1996)

studied the NTSI numerically and found that the shear flows yielded by the momentum transfer due to the NTSI trigger KHI modes, which constitute the main cause of the internal structure of the slab. Klein & Woods (1998) partially included the effect of magnetic fields by considering only the effect of the magnetic pressure in their study of the NTSI in the context of cloud formation by colliding flows and found that the NTSI provides a new mechanism for the generation of filamentary structure. Hueckstaedt (2003) studied the effect of gravity and strong cooling on the NTSI, finding that strong cooling can fuel the growth of the NTSI due to the stronger compression, but it could also lead to KHI modes that can suppress its development. Recently, Heitsch et al. (2007) studied the magnetic nonlinear thin-shell instability (NTSI) numerically using isothermal MHD simulations. In this work, it is found that a magnetic field aligned with the inflow weakens the NTSI.

2.3.4. Gravitational Instability

The gravitational instability is important for dense gas and star formation in the ISM. Jeans (1902) studied this instability assuming a uniform gas cloud in spherical geometry, with initial density ρ_0, and a sound speed c_s. The initial configuration of this region is perturbed, and the self-gravity of the perturbed density region works against the pressure gradient that opposes the collapse. He found a characteristic length important for the collapse called the Jeans' length ($L_{\rm J}$), which is given by

$$L_{\rm J} = \sqrt{\frac{\pi c_{\rm s}^2}{G\rho_0}}, \tag{2.36}$$

where G is the gravitational constant. The main result of this study was that when the wavelength of the perturbation is larger than $L_{\rm J}$ the structure is unstable and collapses. On the other hand, when the wavelength is less than $L_{\rm J}$, the structure is stable and oscillates around the equilibrium state.

Another way to describe this instability is by defining the mass of the spherical distribution with a diameter equal to the $L_{\rm J}$, the Jeans' mass

$$M_{\rm J} = \frac{\pi\rho_0}{6}\left(\frac{\pi c_{\rm s}^2}{G\rho_0}\right)^{3/2}. \tag{2.37}$$

The gravitational instability has a characteristic time that measures the necessary time for the collapse of the structure called the free-fall time (e.g. Binney & Tremaine, 2008). For the assumptions described above, it is

$$\tau_{\rm ff} = \left(\frac{3\pi}{32G\rho_0}\right)^{1/2}. \tag{2.38}$$

In this Ph.D. project, the gravitational instability is important for Chapter 3, where we propose a new resolution criterion for the adequate numerical solution of magnetic support against gravity in molecular clouds.

3

A Resolution Criterion based on Characteristic Timescales for MHD Simulations of Molecular Clouds

3.1. Introduction

In this Chapter, we present the results of the first part of this Ph.D. thesis. Here, we investigate the effect of numerical magnetic diffusion in magnetohydrodynamic (MHD) simulations of magnetically supported molecular clouds. To this end, we have performed numerical studies on adaptive mesh isothermal simulations of marginally subcritical molecular clouds.

As mentioned in Section 2.1.2, the standard approach to obtain a resolution criterion is by convergence test, which consists in increasing the numerical resolution until a physical property remains constant. This kind of approach lacks physical motivation. In contrast, in this project, we propose a physically motivated resolution criterion based on the determination of the numerical magnetic diffusion coefficient and the comparison of the obtained magnetic diffusion time with the relevant dynamical time.

In the rest of this chapter, we present the simulations, results, discussions, and conclusions. An explanation of numerical diffusion, the relevant literature, and numerical resolution criteria can be found in Sections 2.1.1 and 2.1.2, respectively.

3.2. Molecular Cloud Simulations

3.2.1. Numerical set-up

In this section, we present a suite of three-dimensional numerical simulations of magnetic support in molecular clouds using the adaptive mesh refinement (AMR) code FLASH, version 4.5, (Fryxell et al., 2000; Dubey et al., 2008; Dubey et al., 2009) , and the ideal magnetohydrodynamic (MHD) multiwave Harten HLL-type solver (Waagan et al., 2011). The gravitational solver applied for these simulations is an OctTree algorithm also included in FLASH, which can be used to calculate the gas self-gravity (Wünsch et al., 2018), while for the adaptive refinement, we use the Löhner's error estimation applied to the density (Lohner, 1987).

Table 3.1: Molecular cloud simulations. In the first, second, and third columns the simulation's name, its effective and maximum resolution is shown. In the fourth column, we show the magnetic pressure gradient magnitudes computed at half the Jeans' length. The diffusion coefficients, free-fall times, diffusion times, and collapse times at the dynamically equivalent time (see text) are shown in the fifth, sixth, seventh, and eight columns respectively. Note that the computation process to obtain the diffusion coefficients is described in Section 3.5.1.

Simulation	Effect. resolution	Max. resolution (pc)	$\lvert\nabla P_B\rvert$ (dyn/cm^3)	η (pc^2/ Myr)	τ_{ff}(Myr)	τ_d (Myr)	τ_{coll} (Myr)
MC7	128	7.81×10^{-2}	1.565×10^{-29}	0.293	0.428	0.083	9.6
MC8	256	3.91×10^{-2}	1.041×10^{-29}	0.036	0.353	0.384	9.8
MC9	512	1.95×10^{-2}	1.218×10^{-30}	0.001	0.697	51.907	–

We consider an isothermal cloud that is marginally supported by the magnetic field (i.e. marginally subcritical), and find the minimum numerical resolution necessary for the cloud to actually be supported, rather than collapsing due to the loss of magnetic support caused by numerical diffusion. Each of these simulations has the same initial conditions and starts with an initial effective resolution of 32 cells per dimension, although each simulation reaches a different maximum resolution (see Table 3.1). They also include periodic boundary conditions for both the magnetohydrodynamics and the self-gravity.

The initial conditions consist of an initially uniform magnetic field along the x-axis of 25.17 μG, a box size of 10 pc, and a density perturbation of a 3D Gaussian profile on top of a background density ρ_0:

$$\rho = \rho_0 \left\{ 1 + A \ \exp\left[-\frac{1}{2\sigma^2}\left(x^2 + y^2 + z^2\right)\right]\right\}, \tag{3.1}$$

where A and σ are constants that represent the perturbation amplitude and a measure of the perturbation size respectively. For this simulation, $\rho_0 = 2.12 \times 10^{-22}\,\mathrm{g\,cm^{-3}}$, $A = 1.50$, $\sigma = 2.5$ pc. This setup results in a total mass in the computational volume of $4.14 \times 10^3 M_\odot$, a Jeans' length of 2.66 pc, given by

$$L_\mathrm{J} = \sqrt{\frac{\pi c_\mathrm{s}^2}{G\rho}}, \tag{3.2}$$

where $c_s = 0.2\,\mathrm{km\,s^{-1}}$ is the sound speed, and a mass-to-flux ratio $\mu = 0.53$ where we considered spherical geometry.

It is important to notice that this estimated value for the mass-to-flux ratio ($\mu = 0.53$) yields in practice a marginally subcritical molecular cloud because it neither includes the contribution of the external gas and magnetic pressures on the computation of the critical mass-to-flux ratio (Shu, 1992) nor the flat geometry of the cloud due to the mass accretion along the magnetic field lines (Strittmatter, 1966). The marginal nature of the subcritical condition is an important feature since otherwise, the cloud evolution should not be very different for simulations with similar numerical resolutions.

3.2.2. Results of the Simulations

As mentioned in the previous section, the three simulations have identical physical parameters and differ only in the maximum resolution allowed in each of them. We find that, while the low (MC7) and medium resolution (MC8) simulations undergo collapse after 9.6 and 9.8 Myr,

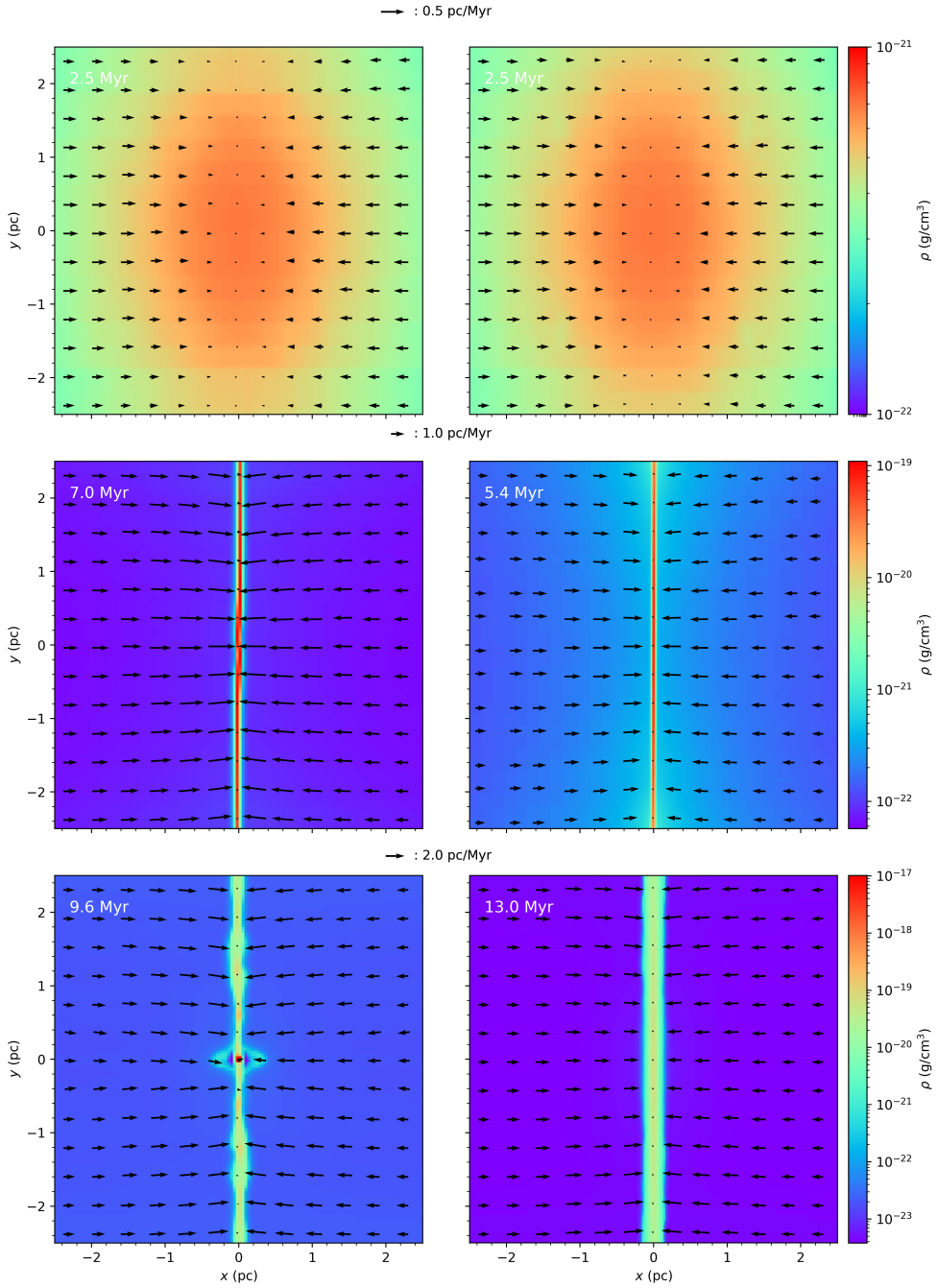

Figure 3.1: Zoomed cross section through the $z = 0$ plane. Colors represent gas density and the velocity field is represented by the black arrows. Left-hand column corresponds to the MC8 simulation while right-hand column to the MC9 simulation. Note the different evolution times for each simulation. Simulation MC8 has already developed a collapsed object at its center by $t = 9.6$ Myr, while run MC9 has not done it even by $t = 13.0$ Myr.

respectively, a dense structure is formed and oscillates around an equilibrium state for the high-resolution run (MC9).

The evolution of the intermediate (MC8) and high-resolution (MC9) simulations are shown in Figure 3.1.[1] Both simulations start their evolution in a very similar way (top left and top right panels), collecting gas on the central part of the computational domain along the magnetic field direction. The maximum density in both simulations increases and eventually reaches a plateau on its temporal evolution which is shown in Figure 3.2. The time to reach the plateau density value is different in each simulation. We attribute this to the presence of different levels of numerical diffusion at each resolution so that magnetic support is lost more rapidly at lower resolutions.

Therefore, we consider a different but dynamically equivalent time in each simulation, defined as the first time in which the temporal evolution of the maximum density's slope reaches a minimum positive because, at this stage, the subcritical clouds would start oscillating around an equilibrium state if the numerical diffusion is negligible, which is what happens in the plateau stage for the simulation MC9 shown in Figure 3.2. We call this stage the dynamically equivalent for the different simulations. The dynamically equivalent times are 7.8, 7.0, and 5.4 Myr for the simulations MC7, MC8, and MC9 respectively, and we consider them as the computation snapshots for the diffusion and dynamical times estimates (see Section 3.5.3). Note that the uncertainty of the dynamically equivalent times does not significantly affect the results of this work since near these regions there is a very small variation in ρ_{max} (see Figure 3.2). As a consequence, there is little influence of the dynamically equivalent time in the computed free-fall time for each of the simulations. In addition, the numerical diffusion time does not depend on the density (See Section 3.3).

After the dynamically equivalent stage, the final evolution state of each simulation depends on whether the resolution was enough for solving the magnetic field correctly or not. For MC8, as shown in the bottom left panel of Figure 3.1, the structure collapses due to the poor numerical resolution, or equivalently, to its high numerical magnetic diffusion coefficient. On the contrary, as shown in the bottom right panel of this figure, MC9 oscillates around an equilibrium state without collapsing in agreement with its subcritical condition. Therefore, numerical diffusion of the magnetic field can cause a spurious collapse of a marginally sub-critical molecular cloud.

3.3. Resolution Criterion

In the previous section, we empirically found the resolution necessary to properly resolve the magnetic support of a subcritical molecular cloud. However, it would be desirable to have a more physically motivated, predictive criterion that can then be used in simulations in regard to effects other than the magnetic field. Since the evolution of any physical process is controlled by its relevant dynamical time, we propose a resolution criterion based on comparing the numerical diffusion time in a given simulation to the dynamical time of the physical process under investigation.

For subcritical molecular clouds, we obtain the relevant dynamical times from the condition $\mu < 1$, which requires that the Alfvén crossing time be less than the free-fall time:

$$\tau_{\rm A} < \tau_{\rm ff}, \tag{3.3}$$

[1]This and the other plots present in this manuscript were done using yt project (Turk et al., 2011).

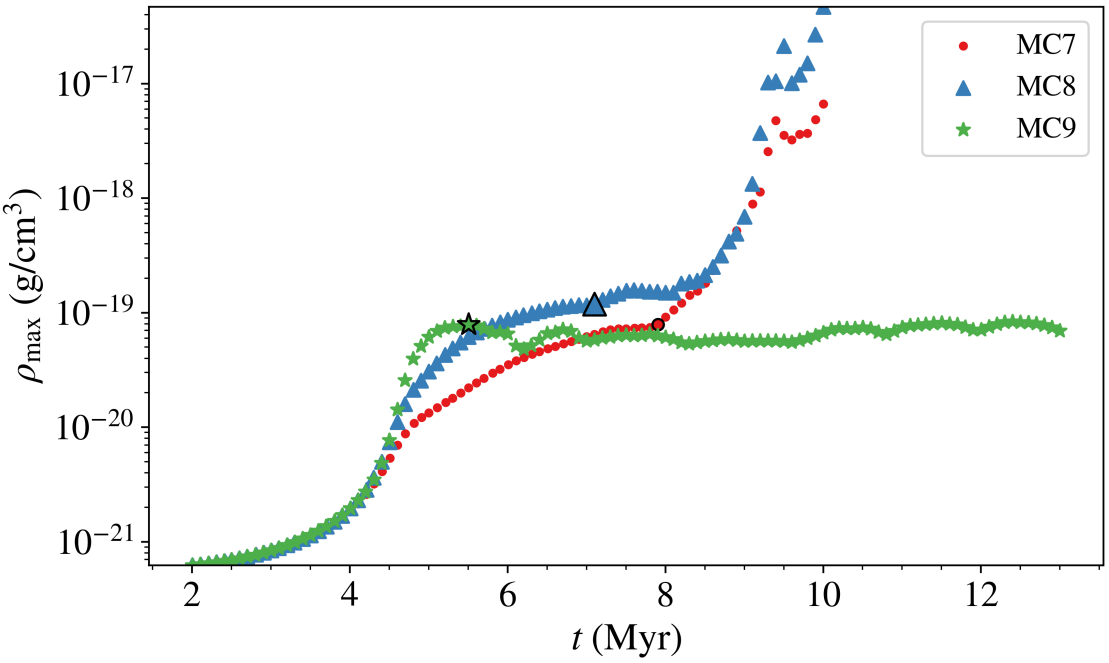

Figure 3.2: Temporal evolution of the maximum density in each of the MC simulations. The dark edge-colored ●▲, ★ represent the dynamical equivalent densities for the MC7, MC8, and MC9 simulations respectively.

where the Alfvén crossing time is given by

$$\tau_{\rm A} = L/u_{\rm A}, \tag{3.4}$$

with L being the relevant spatial scale and $u_{\rm A}$ the Alfvén velocity. In turn, the free-fall time is given by

$$\tau_{\rm ff} = \left(\frac{3\pi}{32G\rho}\right)^{1/2}, \tag{3.5}$$

where G is the gravitational constant. To obtain the resolution criterion, we compare the diffusion time with these time scales.

The diffusion time in the simulation may be obtained using the fact that the effect of the spatial discretization due to the numerical grid on the evolution of magnetic fields can be computed in terms of a magnetic diffusivity coefficient η (e.g., Bodenheimer, 2007). Hence, a diffusion time may be computed in terms of η,

$$\tau_{\rm d} = L^2/\eta, \tag{3.6}$$

where η is the numerical magnetic diffusion coefficient. So, a smaller η means a larger diffusion time; ideal MHD is achieved when it is equal to zero.

When the numerical magnetic diffusion is large and controls the dynamics of the structure, we have

$$\tau_{\rm d} < \tau_{\rm A}. \tag{3.7}$$

In this case, the evolution of the structure is not physical because it is driven by numerical diffusivity and the Alfvén waves up to the wavelength for which $\tau_{\rm d} = \tau_{\rm A}$ are damped by numerical diffusion.

Increasing the numerical resolution reduces the numerical magnetic diffusion coefficient, so, the numerical magnetic diffusion time given by equation (3.6) increases. Therefore, the numerical resolution should be increased until the numerical diffusion and dynamical times fulfill the relation

$$\tau_{\rm ff}, \tau_{\rm A} < \tau_{\rm d}. \tag{3.8}$$

When relation (3.8) is satisfied, the diffusion time is larger than the dynamical time of the mechanism responsible for the support of the molecular cloud, namely the propagation of MHD waves, for which the relevant time-scale is the Alfvén crossing time. Therefore, when relation (3.8) is satisfied, Alfvén waves can propagate without significant numerical diffusion during a free-fall time[2], and thus our proposed resolution criterion based on the characteristic time-scales of the problem consists of finding a numerical resolution that ensures that relation (3.8) is satisfied. The problem becomes now the estimation of the numerical diffusion time-scale as a function of resolution.

3.4. Harris-like Current-sheet Simulations

In order to apply the resolution criterion given by relation (3.8), we first need to measure the numerical magnetic diffusion coefficient η. With this in mind, we simulate a Harris-like current-sheet (e.g., Skála et al., 2015; Kliem et al., 2000). This simulation consists in setting up a magnetic field configuration that reverses direction across a narrow region, maintaining total (thermal + magnetic) pressure equilibrium. Following the set-up of Skála et al. (2015), these simulations are two-dimensional and isothermal with a computational domain of $[-5,\ 5]$ pc on the x-axis, $[-0.6,\ 0.6]$ pc on the y-axis, and open and periodic boundary conditions in the x and y directions, respectively. Note that these simulations do not include self-gravity.

The initial density and magnetic field intensity is given by

$$\rho = \left(P_{\rm tot} - P_{B,{\rm par}}\ \tanh^2(x)\right)/c_{\rm s}^2, \tag{3.9}$$

$$B_y = \left(8\pi\ P_{B,{\rm par}}\right)^{1/2} \tanh(x), \tag{3.10}$$

where $P_{\rm tot} = P_{\rm th} + P_B$ is the total pressure, $P_{\rm th} = c_{\rm s}^2\rho$ is the thermal pressure, and $P_B = B^2/8\pi$ is the magnetic pressure. $P_{B,{\rm par}}$ is the asymptotic value of the magnetic pressure at large x.

Numerical magnetic diffusion disrupts the initial pressure equilibrium in the central region of the computational domain, which is the region where the gradient of the magnetic field is the largest. In order to measure the magnetic diffusion coefficient on this region, we consider the induction equation in the presence of resistivity:

$$\frac{\partial \boldsymbol{B}}{\partial t} + \nabla \times (\boldsymbol{B} \times \boldsymbol{u}) = -\nabla \times (\eta \nabla \times \boldsymbol{B}), \tag{3.11}$$

[2]Note that we will actually consider *twice* the free-fall time as the relevant time-scale because numerical simulations consistently show this to be the order of the actual collapse time, since the thermal pressure gradient is not negligible during the first stages of the collapse (e.g., Larson, 1969; Galván-Madrid et al., 2007; Naranjo-Romero et al., 2015).

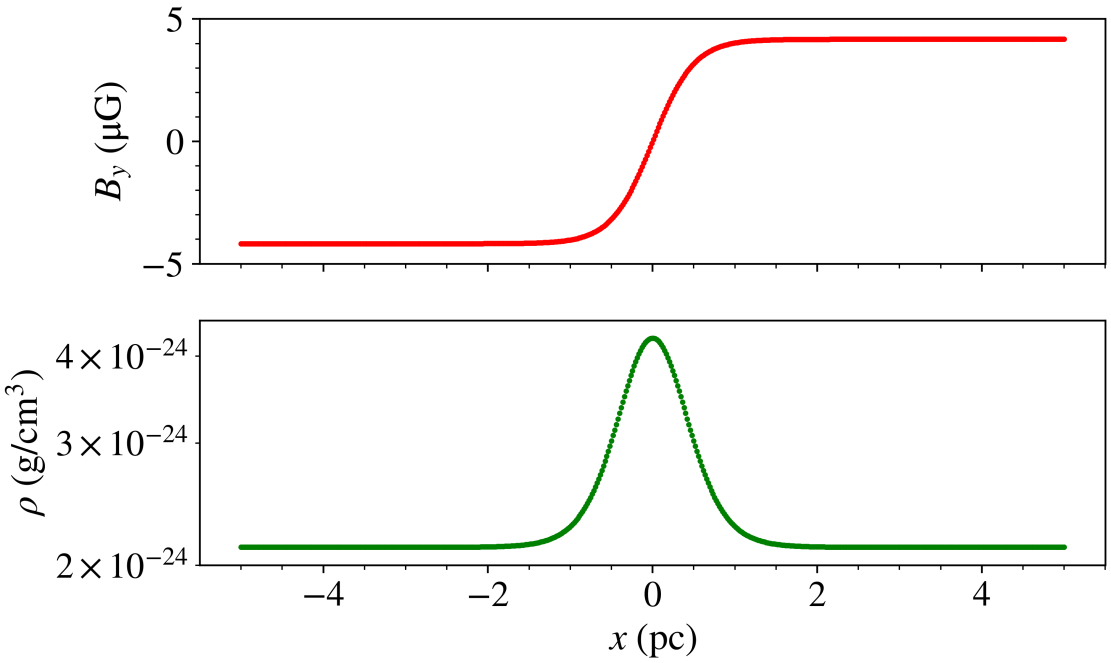

Figure 3.3: Magnetic field and density initial conditions for the Harris-like simulations.

where $\boldsymbol{u}$ is the fluid velocity, which, for our pressure equilibrium configuration, is zero. Assuming that η is uniform in space, we obtain

$$\eta = \frac{\left(\frac{\partial B}{\partial t}\right)}{\left(\frac{\partial^2 B}{\partial x^2}\right)}. \tag{3.12}$$

Hence, in order to measure the numerical resistivity corresponding to a given resolution, we performed the suite of simulations with a uniform grid, different numerical resolutions, and the same initial conditions described in Table 3.2. The simulations were performed with the same version of the FLASH code and MHD solver described in Section 3.2.1. With this set of simulations, we are able to estimate η with equation (3.12). Note that the derivatives appearing in this equation have to be computed in a position where it is possible to solve for η in equation (3.11), i.e., in a position where $\partial^2 B/\partial x^2 \neq 0$.

3.5. Results

3.5.1. Numerical Magnetic Diffusion Coefficients of the Harris-like Simulations

To measure the numerical magnetic diffusion coefficients of each of the simulations presented in Table 3.2, where we have set the initial conditions to obtain the density and magnetic field profiles shown in Figure 3.3. We evaluated numerically equation (3.12) on the point $(x_\mathrm{m},\ y_\mathrm{m}) = (-0.5493\,\mathrm{pc}, 0) \equiv (-x_0,\ 0)$, which is the point where the magnetic field strength is

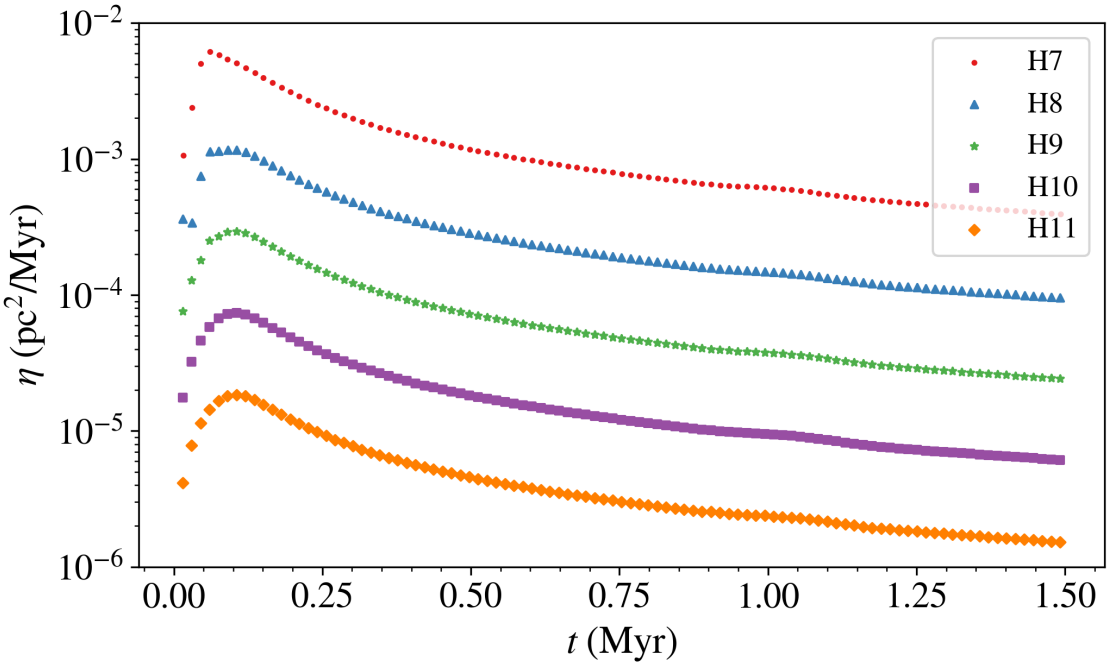

Figure 3.4: η *versus* time for the Harris-like simulations.

half of its maximum magnitude[3]. The magnetic diffusion coefficient measured over time, following the prescription by Skála et al. (2015), is shown in Figure 3.4. As expected, a higher resolution yields a smaller numerical magnetic diffusion coefficient, thus a larger diffusion time.

Since η varies in time, we consider its maximum value at each resolution as the measured value to avoid that the temporal dependence of the denominator dominates its evolution. The resulting numerical diffusion coefficients are listed in the third column of Table 3.2[4], and are plotted in Figure 3.5 together with a fit given by $\log(\eta) = 2.07\log(\Delta x) + 0.04$. Therefore, since η decreases approximately as the square of the numerical resolution for the MHD multiwave Harten HLL-type solver used in this experiment, this dependence implies $\tau_d \propto (L/\Delta x)^2$, so large structures at a given resolution level have large diffusion times, i.e., very small influence of the diffusion of the magnetic field in their evolution.

3.5.2. Scaling of the Magnetic Diffusivity Coefficient for Different Conditions

In addition to depending on the resolution, the value of the numerical magnetic diffusion coefficient depends also on the magnetic field derivatives in the region where it is measured. In order to estimate this dependence, we performed several Harris-like current sheet simulations for a range of values of the magnetic pressure parameter $P_{B,\mathrm{par}}$ (see eq. 3.10) while keeping the same numerical resolution and the same width of the central transition region (i.e., keeping

[3]This point fulfill the condition to solve for η from equation (3.11), i.e., $\partial^2 B/\partial x^2 \neq 0$ (See the previous section).

[4]We also computed the diffusion parameters for the eight-wave MHD solver included in the FLASH 4.5 distribution. These results are shown in Appendix A

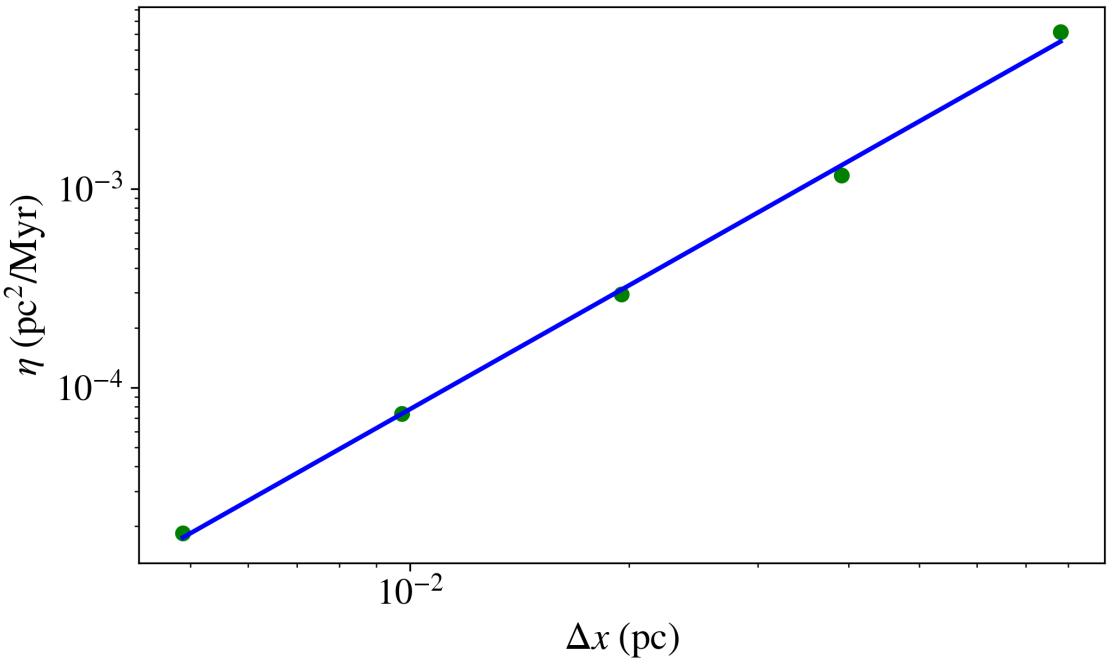

Figure 3.5: Numerical magnetic diffusion coefficient (η) vs numerical resolution (Δx) for the Harris-like current sheet simulations shown in Table 3.2. Note that higher resolution or small Δx implies a smaller numerical magnetic diffusion.

Table 3.2: Harris-like simulations. The first and second columns represent the simulation name and its (uniform) numerical resolution respectively. The third and fourth columns represent numerical magnetic diffusion coefficients and magnetic pressure gradient magnitudes.

Simulation	Resolution (pc)	η (pc^2/ Myr)	$\lvert\nabla P_B\rvert$ (dyn/cm^3)
H7	7.81×10^{-2}	6.164×10^{-3}	3.289×10^{-31}
H8	3.91×10^{-2}	1.170×10^{-3}	3.406×10^{-31}
H9	1.95×10^{-2}	2.950×10^{-4}	3.393×10^{-31}
H10	9.75×10^{-3}	7.399×10^{-5}	3.383×10^{-31}
H11	4.88×10^{-3}	1.849×10^{-5}	3.377×10^{-31}

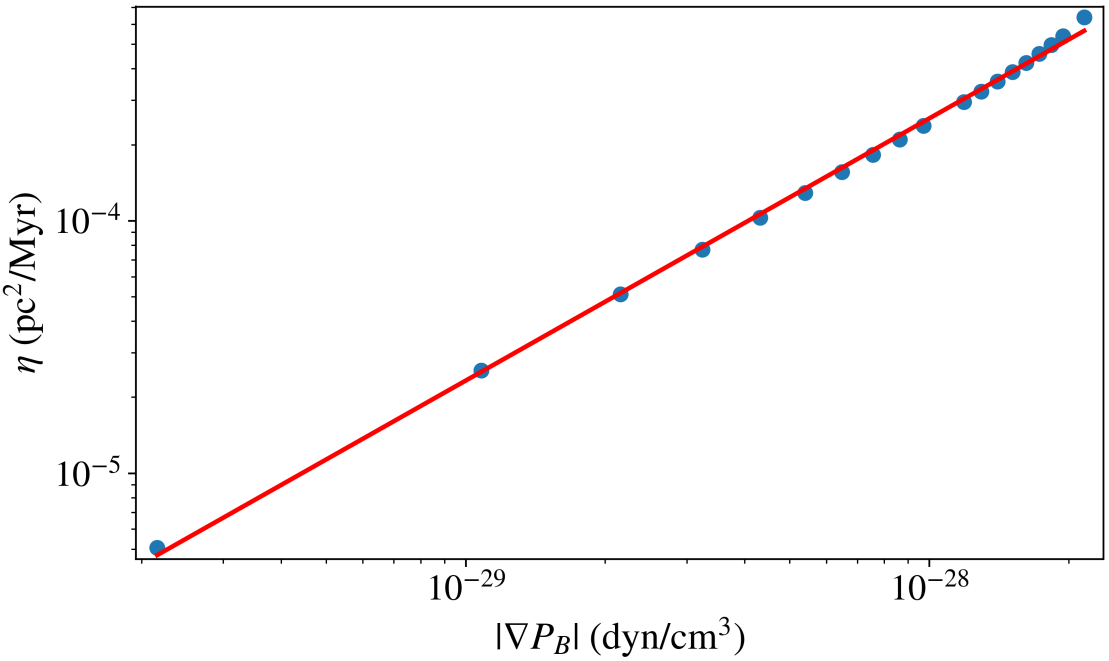

Figure 3.6: The numerical diffusivity η *versus* the magnetic pressure gradient magnitude. The blue points represent the measured values while the red line is a fit to those points.

the same value of x_0) used in simulation H7. Thus, varying $P_{B,\mathrm{par}}$ is equivalent to varying the magnetic pressure gradient since x_0 is kept constant.

For this set of simulations, we chose values of $P_{B,\mathrm{par}}$ that correspond to magnetic field values in the range of [10.56, 105.64] μG. We find that η scales almost linearly with the magnetic pressure gradient, as shown in Figure 3.6, for which we obtained a fit given by $\log(\eta) \approx 25.48 + 1.04 \log(|\nabla P_B|)$. We attribute this behavior to the fact that, in the Harris simulations, the total pressure equilibrium is broken due to the effect of magnetic diffusion in the magnetic pressure gradient. Therefore, we make the ansatz that η depends on ∇P_B, which allows us to incorporate different values of the magnetic field gradient into the computed value for η by making the correction

$$\eta_2 = \eta_1 \frac{|\nabla P_{B2}|}{|\nabla P_{B1}|}, \tag{3.13}$$

where η_2 and η_1 are the numerical magnetic diffusion coefficient under the conditions of magnetic pressure gradient ∇P_{B2} and ∇P_{B1} respectively. In our case, this allows us to use the derived values for η in the Harris-like simulations. We, therefore, proceed as follows: For a given refinement level, the pressure gradient, ∇P_{B1}, is measured at the same point as η_1 (see section 3.5.1) in the Harris-like simulations. These measurements are listed in the fourth column of Table 3.2. In the molecular cloud simulations, ∇P_{B2} is measured at a distance equal to half the Jeans length from the cloud's center since we are studying the evolution of a molecular cloud that would collapse in the absence of magnetic support, therefore, the Jeans length is the relevant characteristic length scale. Therefore, using the measured values for η_1,

$|\nabla P_{B1}|$, $|\nabla P_{B2}|$ (listed in Tables 3.2 and 3.1), as well as equation (3.13), we obtain the values of η_2 also listed in Table 3.1). In turn, this allows us to compute the diffusion time and compare it with the free-fall time to ensure that the numerical resolution is enough to correctly model the dynamical evolution.

3.5.3. Diffusion and Dynamical Times

According to eq. (3.6), the diffusion time-scales can be obtained from the numerical magnetic diffusion coefficients and the spatial scale across which the magnetic field is being diffused. As mentioned in the previous subsection, we consider half the Jeans length as the diffusion length scale. The diffusion and free-fall times are computed at the time when the simulations reach their dynamically equivalent state (see Section 3.2) and are listed in Table 3.1. It is worth noting that the computed free-fall times differ only slightly for the different resolution simulations, while the estimated diffusion times vary by almost 3 orders of magnitude, as a consequence of the strong dependence of the magnetic diffusion coefficient on numerical resolution. Specifically, for the MC7 and MC8 simulations, the diffusion time is smaller than twice the free-fall time. In other words, the numerical diffusion of the magnetic field controls the dynamics of these clouds. Unsurprisingly, the subcritical cloud spuriously collapses.

In contrast, for the MC9 simulation, the diffusion time is larger than twice the free-fall time. So, this simulation is not dominated by the numerical diffusion of the magnetic field and it does not collapse.

In conclusion, the results from this section show that our resolution criterion, based on comparing the numerical diffusion time scale with the characteristic time-scale of the physical problem, is consistent with the resolution empirically found to be necessary in order to correctly simulate the magnetic support of a cloud in Section 3.2.

3.6. Discussion and Conclusions

In this work, we have found that a numerical simulation of a marginally magnetically subcritical molecular cloud undergoes spurious collapse if the numerical resolution is insufficient, and presented two different approaches to estimate the resolution required in order to properly resolve the magnetic support. The first one consisted in increasing the maximum resolution level until finding the one that produces the correct physical evolution of a subcritical cloud. The second approach consisted in the implementation of a physically motivated resolution criterion, relying on the comparison of the numerical magnetic diffusion time implied by the resolution used with the relevant dynamical time, in this case, (twice) the free-fall time.

This criterion recovers the required resolution, but in addition, it provides a physical interpretation and a *predictive* procedure for the choice of the required resolution for a given physical process and solver, provided some additional numerical tests are performed such as the Harris-like current sheet simulations to estimate the numerical diffusion at a given numerical resolution, and to obtain the scaling of estimated diffusion coefficients for different magnetic field conditions.

It is important to note that, in this work, we have restricted our study to the effect of numerical magnetic diffusion on the evolution and collapse of subcritical molecular clouds. On the other hand, in the case of supercritical clouds with $\mu > 1$, the relation between the

free-fall and the Alfvénic crossing times corresponding to that presented in equation (3.3) becomes instead

$$\tau_{\rm ff} < \tau_{\rm A}. \tag{3.14}$$

In this case, collapse always occurs but, if the resolution is insufficient, the collapse may occur too rapidly, since it is known that the magnetic forces can in principle delay it (e.g., Ostriker et al., 1999a). Thus, the required numerical resolution to avoid this situation is the one that ensures the fulfillment of

$$\tau_{\rm ff} < \tau_{\rm A} < \tau_{\rm d}. \tag{3.15}$$

Therefore, insufficient resolution in either the subcritical or supercritical cases may lead to an overestimation of the star formation rate.

In addition to the physical problems discussed in this work, i.e., gravitationally unstable subcritical and supercritical molecular clouds, there can be other structures where this criterion can be applied. For example, for cold atomic clouds, we have to consider possible dynamical times related to the thermal instability (Field, 1965). According to Field (1965), in the linear regime clumps can grow with dynamical times depending on the scale of the perturbation. For small wave numbers, the structure's growth time (τ_{gt}) satisfies

$$\tau_s < \tau_{gt} \ , \tag{3.16}$$

where τ_s is the sound crossing time. For intermediate and large wave numbers, we have instead

$$\tau_c < \tau_{gt} \ , \tag{3.17}$$

where τ_c is the cooling time (See Figure 2.5). It is also important to mention that at large wavelengths the growth of clumps is affected by thermal conduction but equation (3.17) is still valid. Besides, over the whole range of perturbation wavelengths in the linear regime of the thermal instability, equation (3.17) still applies. Therefore, the growth time could be used as the dynamical time to validate our resolution criterion for resolving the formation of cold atomic clouds by thermal instability.

Finally, it is noteworthy that this resolution criterion, being physically motivated is applicable to any code or solver. In contrast, a resolution criterion performed through an empirical convergence tests with a particular code and solver, is not guaranteed to be applicable to other codes and/or solvers.

4

Understanding Magnetic Field Alignment with Cold Atomic Clouds

4.1. Introduction

In this Chapter, we present the second part of this Ph.D. thesis, in which we investigate the alignment mechanism between the magnetic field and filamentary cold atomic clouds (CACs). To this end, we perform two- and three-dimensional magnetohydrodynamic (MHD) simulations of colliding warm atomic gas flows considering the multi-phase nature and typical conditions of the interstellar medium (ISM) at the Solar Galactocentric radius.

As mentioned in Section 1.5, the alignment between the magnetic field and density structures has been widely observed, but it is not clear how this correlation occurs. In this part of the thesis, we investigate what are the physical processes responsible for the alignment and what is the role they play in the resulting correlation.

In the rest of this chapter, we present the simulations, results, discussions, and conclusions of this project. The physical processes relevant to the alignment and the relevant literature are explained in more detail in Sections 1.5, 2.2, and 2.3.

4.2. Cold Atomic Cloud Formation Simulation

We have performed 2D and 3D numerical simulations of cold atomic clouds formed by the collision of warm atomic gas flowing along the x-axis and colliding in the center of the computational domain. The simulations were performed using the adaptive mesh refinement (AMR) code Flash version 4.5 (Fryxell et al., 2000; Dubey et al., 2008; Dubey et al., 2009), and the ideal magnetohydrodynamic (MHD) multi-wave HLL-type solver (Waagan et al., 2011). Since our goal is to study the alignment of the magnetic field with weakly self-gravitating CACs, neither self-gravity nor any external gravitational potential are included in these simulations. These simulations consider inflow boundary conditions along the x-axis and periodic boundary conditions for the other axes.

The initial conditions for both kinds of simulations consist of gas in thermal equilibrium with temperature $T_0 = 5006.25\,^{\circ}\mathrm{K}$, implying a sound speed $c_{s,0} = 7.36\ \mathrm{km\ s^{-1}}$, and an atomic hydrogen number density $n_{H,0} = 1\,\mathrm{cm^{-3}}$. For the 3D simulation, the box size of the simulation is $L = 64\,\mathrm{pc}$, the gas inside a cylinder of radius $R = 16\,\mathrm{pc}$, length $\ell = 64\,\mathrm{pc}$, and centered in

the middle of the computational domain, has a velocity $u_0 = \pm 14.7\,\mathrm{km\ s^{-1}}$ in the x direction to the left and right from the $x = 0$ plane, respectively. For the 2D simulations, the box size is $L = 20\,\mathrm{pc}$, and the main difference is that the velocity colliding flows in this simulation include an interface with a sinusoidal shape at the center of the domain in order to trigger the nonlinear thin-shell instability (NTSI) described in Vishniac (1994). This interface is accomplished by requiring that simulation points with $x < 3.0\sin(\frac{8\pi y}{20})\,\mathrm{pc}$ and $x > 3.0\sin(\frac{8\pi y}{20})\,\mathrm{pc}$ have a velocity $u_0 = \pm 14.7\,\mathrm{km\ s^{-1}}$ respectively.

In addition, for the 3D simulation, we add a pseudo-random perturbation to each velocity component while the 2D simulations do not consider velocity perturbations. These initial conditions imply an initial Mach number of $M_\mathrm{s} = 2.0$ for both the 2D and 3D simulations. Furthermore, both kinds of simulations incorporate the multi-phase nature of the interstellar medium by including the net cooling function provided in Koyama & Inutsuka (2002), with the typographical corrections given in Vázquez-Semadeni et al. (2007).

This set of simulations also includes a non-magnetic 2D simulation. For the magnetic 3D and 2D simulations, the initial magnetic field is $B_0 = 3\,\mu\mathrm{G}$ along the x-axis, implying an initial Alfvénic Mach number, given by

$$M_\mathrm{A} = \frac{u_0}{u_\mathrm{A}}, \tag{4.1}$$

of $M_\mathrm{A} = 2.25$, where u_0 is the gas velocity magnitude, $u_\mathrm{A} = B_0/\sqrt{4\pi\rho_0} = 6.54\,\mathrm{km\ s^{-1}}$ is the Alfvén speed, with $\rho_0 = \tilde{\mu} m_H n_{H,0}$, $\tilde{\mu} = 1.27$ being the mean atomic mass. The magnetization of this simulation results in a plasma β of

$$\beta^1 = \frac{c_\mathrm{s}^2}{u_\mathrm{A}^2} = 1.27. \tag{4.2}$$

Therefore, the initial condition of these simulations is supersonic, super-Alfvénic, and with intermediate magnetization.

In Figure 4.1, we show face-on and edge-on column densities of the resulting evolution after 5 Myr. In the following discussion, the highlighted white region located in $x \in [-3.0, 3.0]$ pc, $y \in [-1.0, 3.0]$ pc, and $z \in [2.3, 6.3]$ pc will be referred to as R1. In Figure 4.2[2], we show this region including its three-dimensional density structure and magnetic field lines[3]. As we can see from this Figure, the shaded external sheets are the shock fronts and constitute the positions along the flow where magnetic field lines start to bend. Additionally, the magnetic field becomes almost perpendicular to its original orientation (x-axis) in some regions.

4.3. Alignment of Magnetic Field Lines with Cold Atomic Clouds

To quantify the alignment of magnetic field lines, we use the *histogram of relative orientations* (HRO; Soler et al. 2013, which is a statistical tool to measure the angle between the magnetic field and the density gradient of structures in the ISM (See the section 1.5), for number

[1]This quantity is defined as the ratio of the thermal and magnetic pressures, which intruduces a factor of 2 in the numerator, however, this additional factor is not often used in the literature.

[2]This and the other three-dimensional figures were done with the help of Pyvista (Sullivan & Kaszynski, 2019).

[3]The code developed to obtain magnetic lines is described in Appendix B.

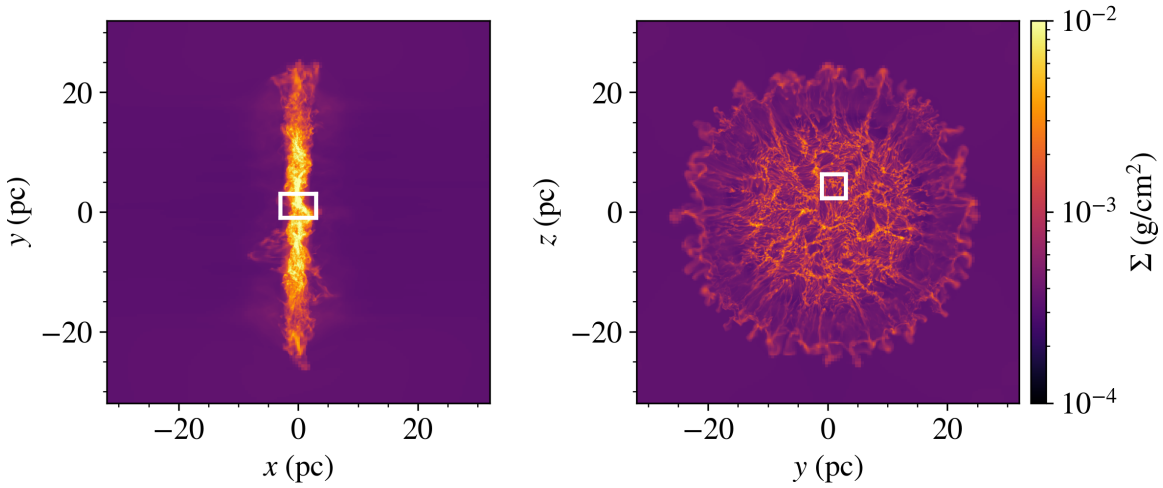

Figure 4.1: Column density of the cold atomic cloud's simulation at 5 Myr. The highlighted region (R1) is examined in 3D in order to show the magnetic field and density morphology.

density intervals[4]relevant to the multi-phase nature of CAC. These number density intervals include the post-shock warm neutral medium ($n \in [3, 10]$ cm^{-3}), low-density cold neutral gas ($n \in [10, 3{\times}10^1]$ cm^{-3}), medium-density cold neutral gas ($n \in [3{\times}10^1, 10^2]$ cm^{-3}), high-density neutral gas ($n \in [10^2, 3 \times 10^2]$ cm^{-3}), and the central densest region ($n \in [3 \times 10^2, 10^3]$ cm^{-3}). We show the resulting HRO in the top panel of Figure 4.3, where we follow the original convention in which ϕ is the angle between the density gradient ∇n and the magnetic field $\boldsymbol{B}$. Thus, when $\cos\phi = 0$, the magnetic field is parallel to the density isocontours, while for $\cos\phi = \pm 1$, the magnetic field is perpendicular to the density isocontours. We keep this original convention to compare to the three-dimensional HRO diagram presented in Soler et al. (2013). We can see that the HRO for all density intervals peak at $\cos(\phi) = 0$; in other words, the magnetic field tends to be parallel to the density structures.

In order to describe the HRO, Soler et al. (2013) introduced the *shape parameter* ζ plotted on the right panel of this figure and defined as

$$\zeta \equiv \frac{A_c - A_e}{A_c + A_e}, \tag{4.3}$$

where A_c is the central area below the HRO diagram located between $\phi \in [75.52°, 104.48°]$, while A_e is the area below the HRO at the extremes values with $\phi \in [0°, 41.41°] \cup [138.59°, 180°]$. Thus for a given density interval, if $0 < \zeta < 1$, the magnetic field lines tend to be parallel to the density gradients, while if $-1 < \zeta < 0$, the magnetic field tends to be perpendicular to the density gradients, and ζ close to zero happens when there is not a clear tendency in the alignment. In the right panel of Figure 4.3, we plot ζ for the simulation in the density ranges defined above, showing that the magnetic field becomes increasingly parallel to the density

[4]Note that in this study, we focus in simulations and do not explore the effects of observational effects like the constrain of only detecting the plane of the sky magnetic field and the relative orientation between the observer and the cloud.

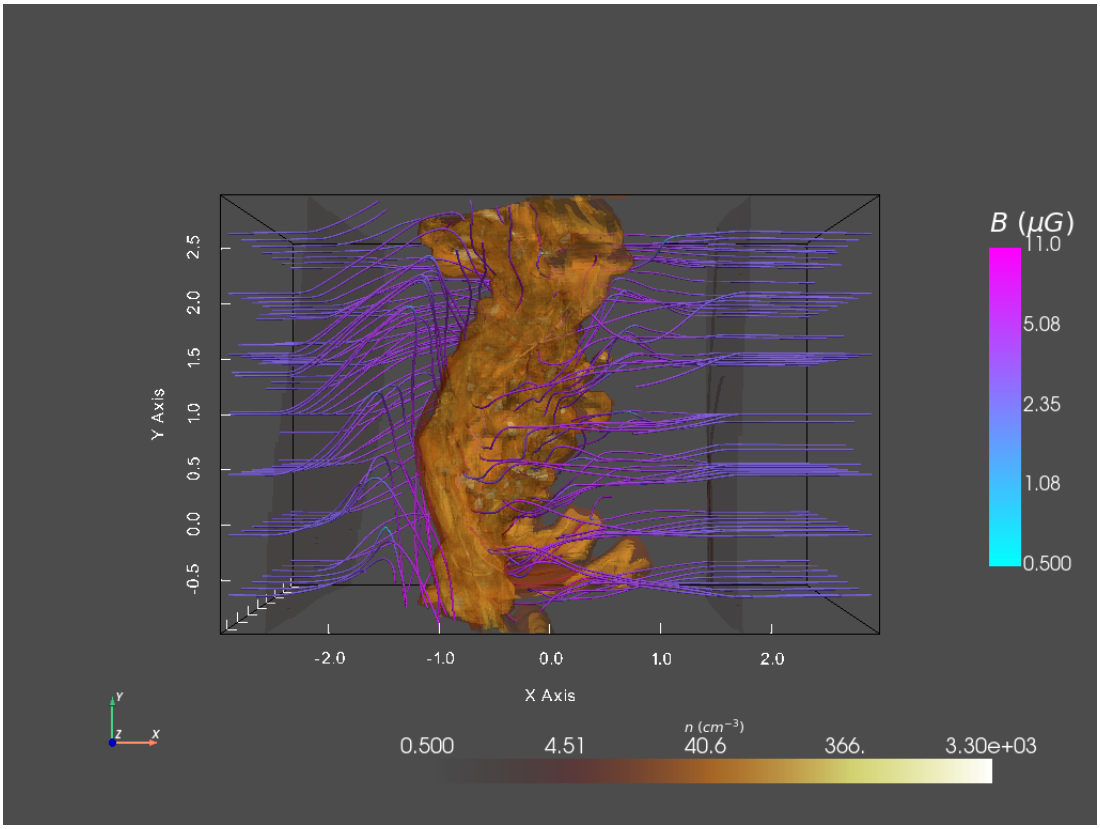

Figure 4.2: The density structure and magnetic field lines of the region R1 are shown after 5 Myr of evolution. Magnetic field lines are colored by their magnitude. Note that at this evolution time, magnetic field lines are almost perpendicular to their original orientation along, the x axis. The dark-shaded regions at both sides of the center are the shock fronts where magnetic field lines start to bend. We provide an animation showing the evolution of this region in the following youtube link.

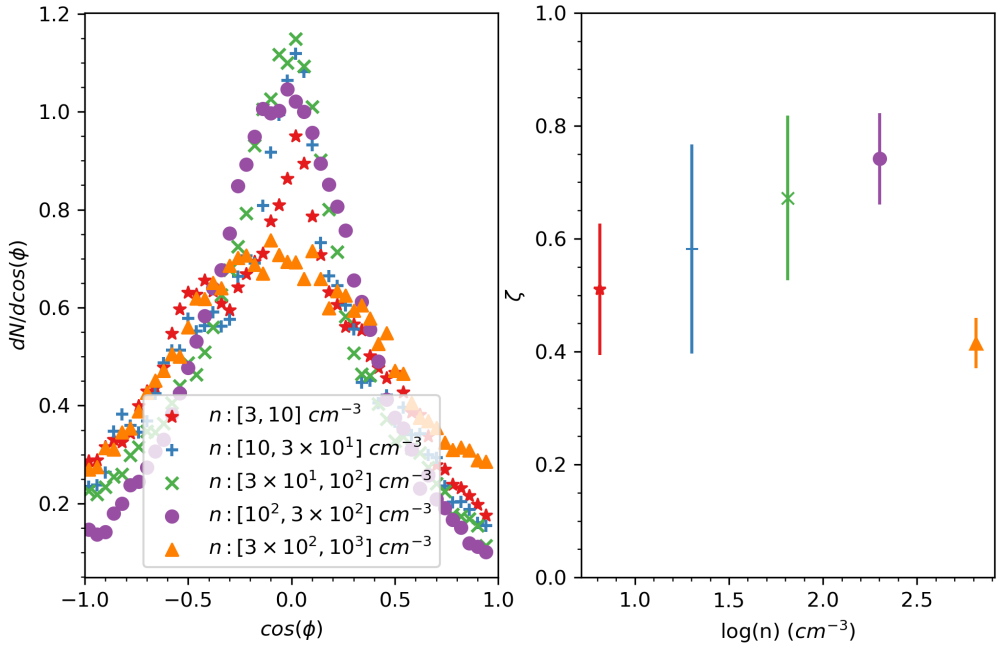

Figure 4.3: Left: HRO diagram for four different number density intervals. Right: shape parameter (see eq. 4.3) versus number density. As we can see in this figure, the magnetic field is increasingly parallel for the first three intervals, but there is a change in the trend for the last interval.

gradient as the density increases up to 3×10^2 cm^{-3}, and the degree of parallel alignment is less for the last interval.

The shape parameters obtained in Figure 4.4 by Soler et al. (2013) indicate that the alignment of the magnetic field and isodensity contours becomes less parallel when increasing the density. In that work, the authors sample density values of $n \in [1.6 \times 10^2, 3.16 \times 10^6]$ cm^3 with isothermal simulations of cold molecular gas. In contrast, since we are focused on how this correlation happens, our simulations start with warn atomic gas leading to density structures with $n \in [6 \times 10^{-1}, 2.2 \times 10^3]$ cm^3. Therefore, the obtained HRO shape parameter in Figure 4.3 complements, and it is consistent with the one obtained by Soler et al. (2013) (See Figure 4.4).

Specifically, the HRO and shape parameter obtained in Figure 4.3 shows an increase in the degree of parallel alignment for the first four density intervals, while for the last one, we can appreciate a change of this tendency towards a non-preferential orientation, which corresponds to the lowest density interval in the results of Soler et al. (2013).

In Figure 4.5, we show the density structures between the four highest density intervals used to obtain the HRO and shape parameter of Figure 4.3. Here, we show the dense structures with three-dimensional isocontours while the magnetic field line is represented with black arrows. As we can see from this figure, the magnetic field lines are parallel to the density structures for the four density intervals. However, for the last one, it is noticeable that in some regions the magnetic field does not follow this general trend, leading to the observed change in the shape parameter.

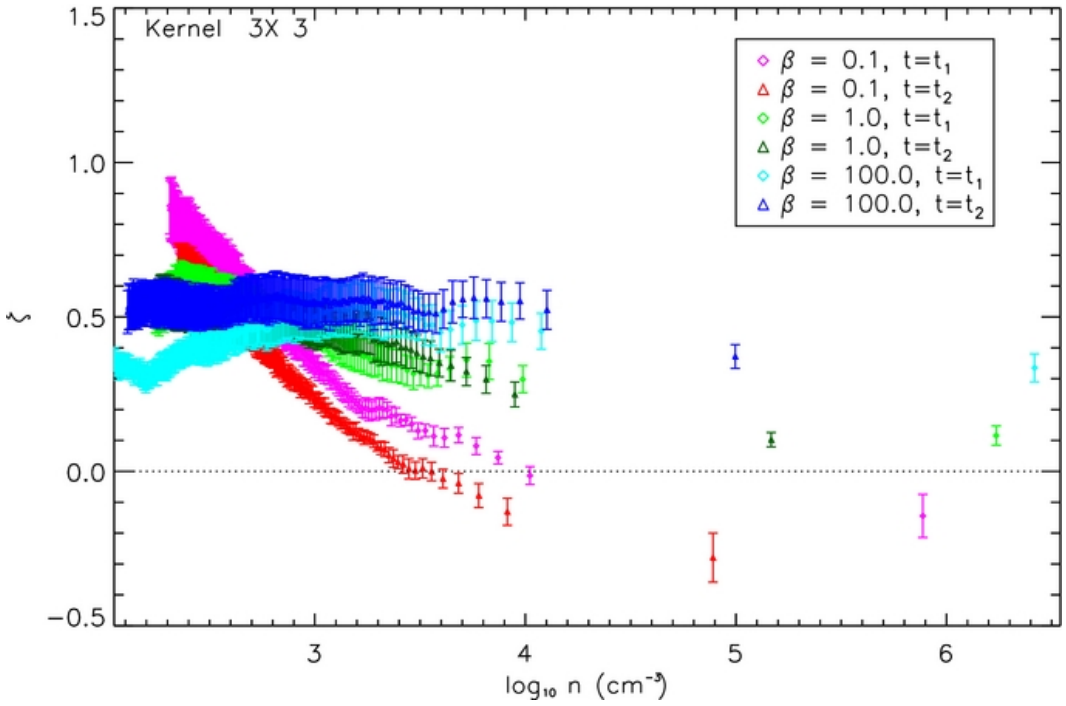

Figure 4.4: HRO shape parameter ζ for the different simulations presented in Soler et al. (2013). Here, $t_1 = 0.585\,\mathrm{Myr}$ and $t_2 = 1.17\,\mathrm{Myr}$. Note that from the simulations with $\beta = 1.0$ are the ones with similar magnetization with our simulations of cloud formation described in Section 4.2

4.4. Magnetic Field Line Evolution

To understand the alignment of the magnetic field with CACs, we followed the evolution of the magnetic field lines. The resulting evolution of region R1 is shown in the animation in Figure 4.2, where we can see the generation of shock fronts at each side of the central condensation region. The magnetic field lines start bending at these shock fronts as they propagate away from the center of the computational domain.

As we can see from the animation, magnetic field lines change their direction from being nearly parallel to the x-axis at early times to being mostly perpendicular to it after 5 Myr. In this section, we explain how this occurs.

4.4.1. Magnetic Field Amplification by MHD Shocks

The magnetic field might amplify its magnitude and change direction due to MHD shocks under certain conditions. MHD shocks are classified according to the geometry of the interaction between the upstream magnetic field and shock front, and the characteristic speeds of the upstream and downstream states.

As mentioned in Section 2.2, shocks can be classified geometrically as parallel, perpendicular, or oblique depending on the angle (θ) between the upstream magnetic field and the vector normal to the shock front. As we can see from Figure 4.2 and considering the shock front located at the right, $\theta \approx 0$ for all the magnetic lines shown, where the shock fronts are the dark layers at both sides of the central region where condensations occur. The small

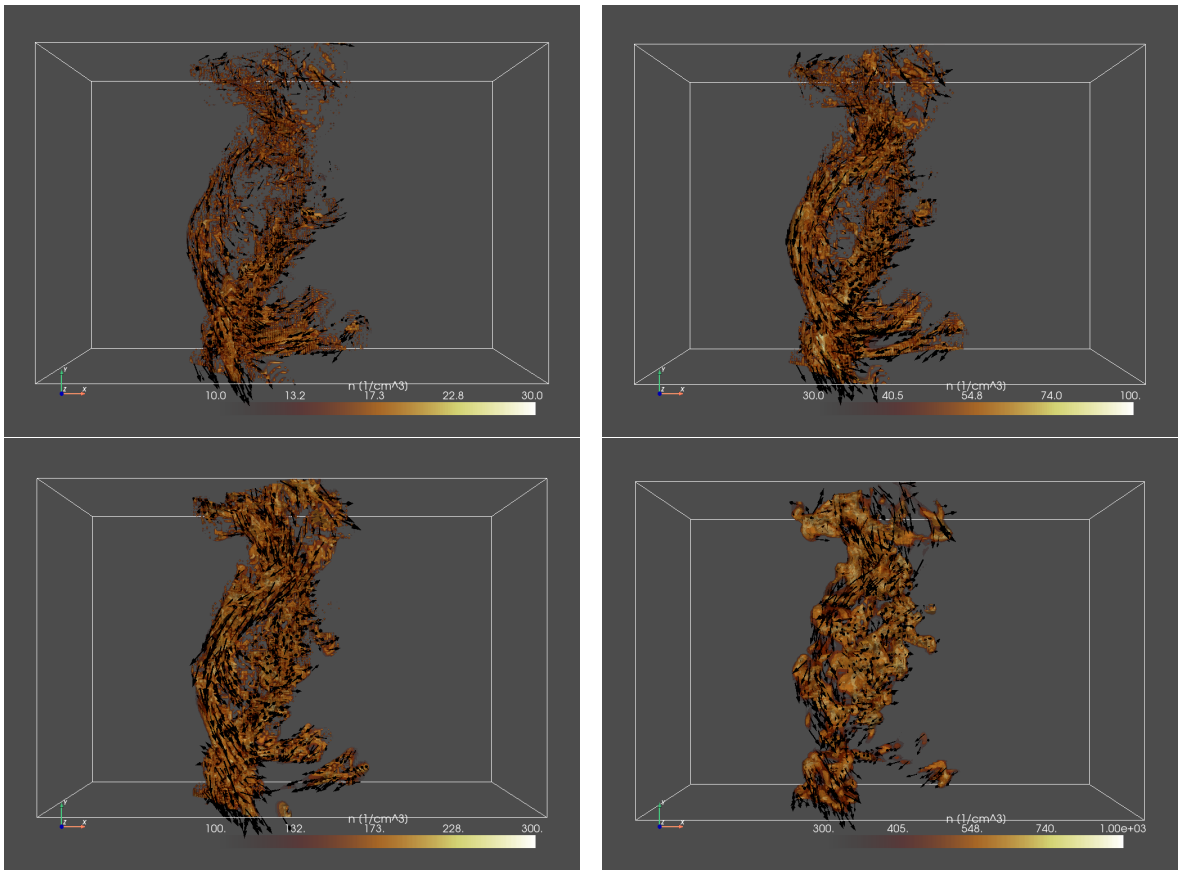

Figure 4.5: Regions used to compute the HRO diagram and the shape parameter shown in Figure 4.3. The yellow surfaces are density isocountours and the dark arrows represent the magnetic field. We can see that for the four density intervals shown here, the magnetic field is noticeably parallel to the density structures. However, the magnetic field shows a deviation from this trend for the highest density interval in the bottom right panel. The top left panel includes $n \in [10, 30]$ cm^{-3} (link 1), the top right panel $n \in [30, 100]$ cm^{-3} (link 2), the botton left $n \in [100, 300]$ cm^{-3} (link 3) , and the botton right $n \in [300, 1000]$ cm^{-3} (link 4). Open the youtube links next to the density intervals to see animations showing each region in detail.

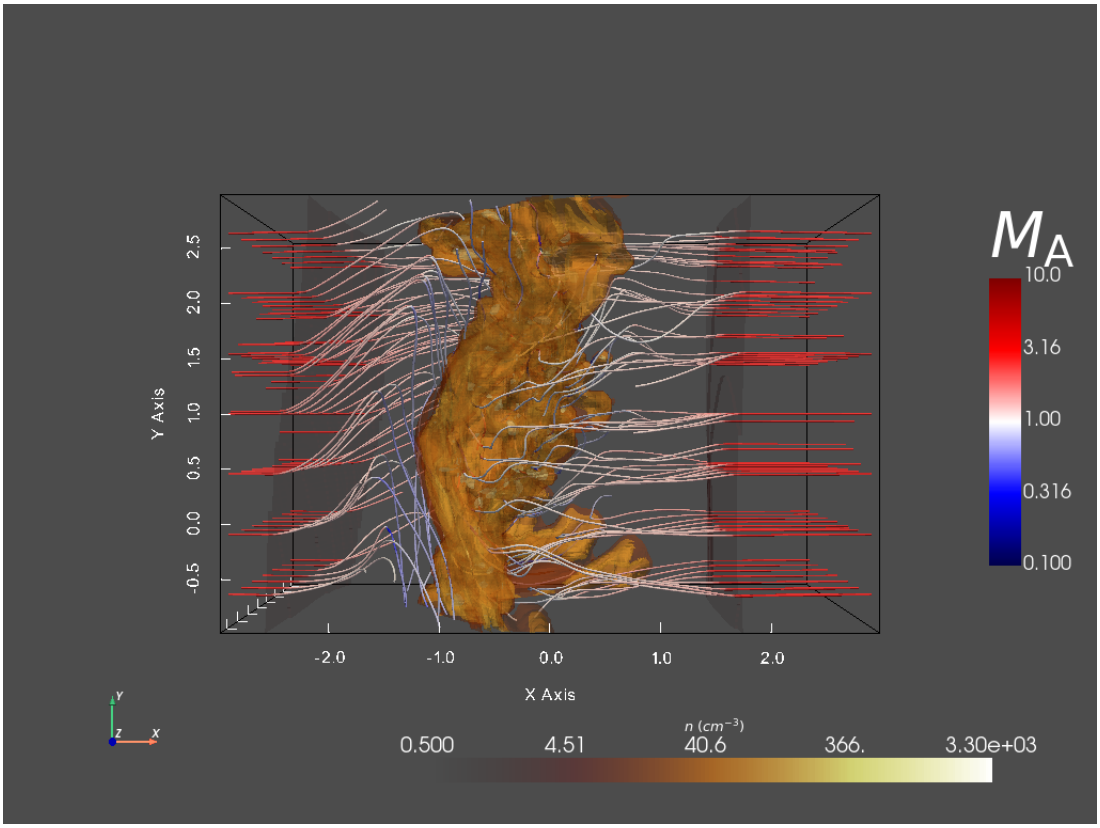

Figure 4.6: Same as Figure 4.2 but with magnetic field lines colored by the Alfvénic mach number. Note the change from super-Alfvénic to trans-Alfvénic of magnetic field lines across the shock. An animation showing the evolution can be found in this youtube link.

variations of θ around zero are due to the fact that the shock front is not a plane when it moves away from the central region because of the fluctuations added to the velocity in the simulation setup.

Shocks may also be classified based on their characteristic speeds. Delmont & Keppens (2011) classify shocks according to their upstream and downstream speeds. They define the fast speed u_f as

$$u_f^2 = \frac{1}{2}(c_s^2 + u_A^2 + \sqrt{(c_s^2 + u_A^2)^2 - 4u_{A,n}^2 c_s^2}), \tag{4.4}$$

where u_A is the Alfvén speed, $u_{A,n}$ is its component normal to the shock front. Considering that u_n is the flow speed normal to the shock, these authors define a flow as *superfast* when $u_f < |u_n|$. In the three-dimensional simulation described in Section 4.2, we have that $u_A \approx u_{A,n}$ because the flow along the x axis can be considered almost perpendicular to the shock front. Therefore from equation (4.4), we obtain $u_f \approx c_s$. Furthermore, from Section 4.2, we know that $u_n = u_0 = 14.7\,\mathrm{km\,s^{-1}}$ and $c_s = 7.36\,\mathrm{km\,s^{-1}}$, and therefore the requirement for a superfast upstream flow is fulfilled. For the downstream flow, just after the shock front, the flow becomes transalfvenic as we can see from Figure 4.6. Therefore the relation $u_{A,n} < |u_n| < u_f$ which characterizes a subfast flow is satisfied downstream. Such MHD shock, going from a superfast to a subfast flow, is called a fast MHD shock (Delmont & Keppens, 2011).

Fast shocks refract the magnetic field away from the shock normal in agreement with the results of our three-dimensional simulation. For fast shocks, the magnetic field amplification of the parallel component to the shock front is given by (See section 2.2.3)

$$B_{\parallel,2} = \frac{r_\rho B_{\parallel,1}(M_{A,1}^2 - \cos^2\theta)}{M_{A,1}^2 - r_\rho \cos^2\theta}, \tag{4.5}$$

where $B_{\parallel,1} = B_1 \sin\theta$ and $B_{\parallel,2}$ are the upstream and downstream magnetic field components parallel to the shock front, $r_\rho = \rho_2/\rho_1$ is the ratio of the downstream (ρ_2) and upstream (ρ_1) densities, $M_{A,1}$ is the Alfvén Mach number of the upstream gas, and θ is the angle between the vector normal to the front-shock and the upstream magnetic field $\boldsymbol{B}_1$. Since this amplification depends on the angle θ, the fluctuating curvature of the shock front at different positions yields the inhomogeneous downstream magnetic field pattern when the shock front travels away from the central region, early in the evolution times (see the animation provided in the caption of Figure 4.2).

4.4.2. Line Bending Model

To understand how magnetic field lines are amplified downstream in the three-dimensional simulations shown in Section 4.2, we developed a simple analytical model based on solving the induction equation in ideal MHD,

$$\frac{\partial \boldsymbol{B}}{\partial t} = -\boldsymbol{B}\nabla\cdot\boldsymbol{u} - (\boldsymbol{u}\cdot\nabla)\boldsymbol{B} + (\boldsymbol{B}\cdot\nabla)\boldsymbol{u}. \tag{4.6}$$

The analytical model consists of a magnetic field line in the downstream or post-shock region that has been perturbed by the passage of a shock front, which amplifies the magnetic field component parallel to it. A sketch representing this perturbed line is shown in Figure 4.7, where we consider that the magnetic field component amplified by the passage of the shock is B_y. In addition, B_x is constant across the shock in agreement with the jump condition for the magnetic field (See equation 2.13). Furthermore, we assume that the flow speed decreases along x, i.e., $u_x = u_x(x)$ and $\partial u_x/\partial x < 0$, which agrees with the compression due to colliding flows. Finally, we disregard the downstream component of the velocity parallel to the shock front, u_y and u_z, to analyze what is the effect of the compression alone.

To validate these assumptions, in Figure 4.8, we plot the relevant physical quantities along a ray parallel to the x axis at 0.7 Myr passing through a region that shows this amplification at later evolution times. In the top panel, the shock front and condensed gas region are clearly marked by the gas density. The middle panel shows that, in addition to the discontinuity at the shocks, the inflow velocity u_x decreases downstream from the shock, developing a negative gradient along x. Also, $u_y,\ u_z \approx 0$, in agreement with our model assumptions. Finally, in the bottom panel, we show that the x component of the magnetic field remains almost constant.

Therefore, making the assumptions $B_y = B_y(x)$, $B_x = C$, where C is a constant, $u_x = u_x(x)$, with $\partial u_x/\partial x < 0$, $u_y, u_z \to 0$, and solving for the B_y component, equation (4.6) reduces to

$$\frac{\partial B_y}{\partial t} = -B_y\frac{\partial u_x}{\partial x} - u_x\frac{\partial B_y}{\partial x}. \tag{4.7}$$

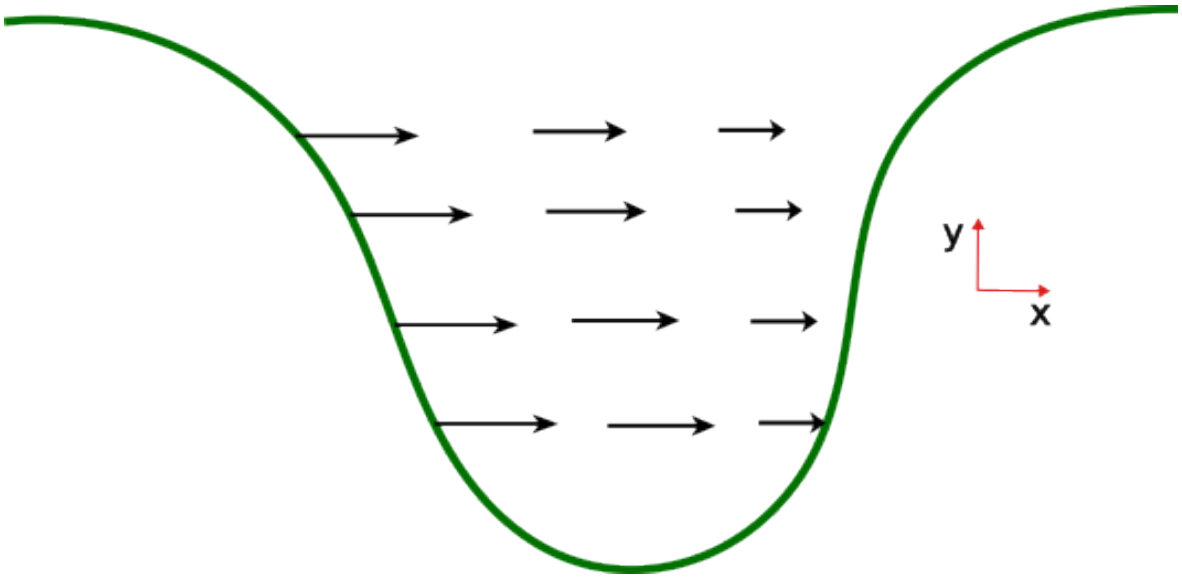

Figure 4.7: Initial line bending model. Magnetic fields are represented by green lines while the velocity field is given by the black arrows.

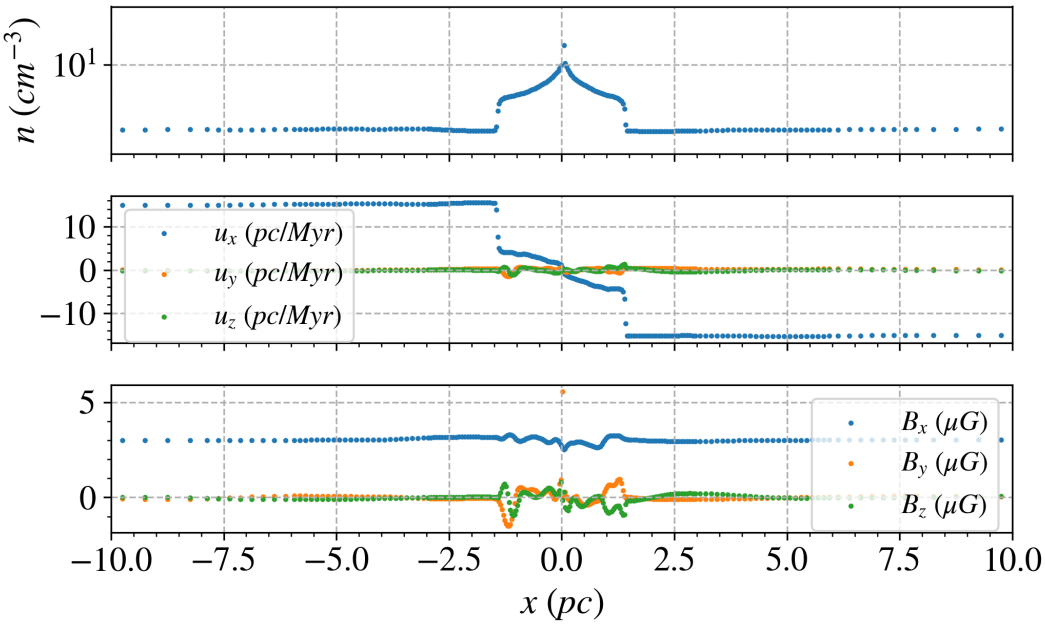

Figure 4.8: Number density (*top*), velocities (*middle*), and magnetic field components (*bottom*) along a ray parallel to the x axis. It can be seen that the profile of these quantities agrees with the line bending model.

This equation can also be written in lagrangian form as

$$\frac{dB_y}{dt} = -B_y \frac{\partial u_x}{\partial x}. \tag{4.8}$$

Thus, taking into account that $\partial u_x/\partial x < 0$ which agrees with the u_x profile along a ray through the x axis shown in middle panel of Figure 4.8, we see that dB_y/dt has the same sign as B_y, and therefore the magnetic field component B_y is amplified by the downstream velocity gradient.

4.5. Discussion

As we have seen from the three-dimensional simulation, magnetic field lines change their orientation at the shock front due to the effect of the fast MHD shock. The passage of the shock front yields an irregular amplification of the parallel component to it, which results in the early downstream shocked magnetic field line pattern. Afterward, magnetic field lines are dragged and folded by the downstream gas motion.

It is important to remark that the analytical solution of shocks, is often presented only in two dimensions, where only the parallel and perpendicular components to the shock front of the physical quantities are considered. The goal of this assumption is to simplify the computations, and it is valid for any pair of dimensions. For example, in Section 4.4.2, we suppose that the components perpendicular and parallel to the shock front are along the x and y axis respectively. However, these results are also valid when the parallel component to the shock front is along the z axis instead of the y axis. We found this is the case in some places of the region R1 as we can see in Figure 4.9, wherein the region $x \in [0.0, 2.0]$ pc, $y \in [3.0, 6.0]$ pc, and $z \in [-1.0, 1.0]$ pc shows the magnetic field amplification in the z direction downstream. In other words, in our 3D simulation, we see field amplification in the two directions parallel to the shock front plane.

In this work, we do not vary the relative orientation between the upstream magnetic field and the shock front of the system in the initial condition. However, there is a small range of angles between them due to the departure of the shock front from a perfectly flat plane due to the velocity fluctuations. The influence of the initial angle between the magnetic field and the shock front is studied in Inoue & Inutsuka (2016), where it was found that the number of CACs or fibers oriented perpendicular to the magnetic field increases with the relative orientation of the upstream magnetic field and the shock front for simulations without an initial velocity dispersion. However, when an initial velocity dispersion is included, the authors find that fibers are more roughly oriented in the direction of the local magnetic field. In this way, they conclude that the formation mechanism of fibers and their alignment with the local magnetic field is the turbulent shear strain, which was also identified as the reason for the elongation of filamentary CACs by Hennebelle (2013). It is important to mention that the role of MHD shocks in the evolution of magnetic field lines that yield the final correlation has not been explored.

One possible source of the turbulent shear strain which produces the elongation of filamentary CACs and the alignment of these structures with the local magnetic field is the NTSI, since it produces the momentum transfer from lateral to longitudinal in the regions around the nodes (See figures 2.8 and 4.11). However, Heitsch et al. (2007) found that when

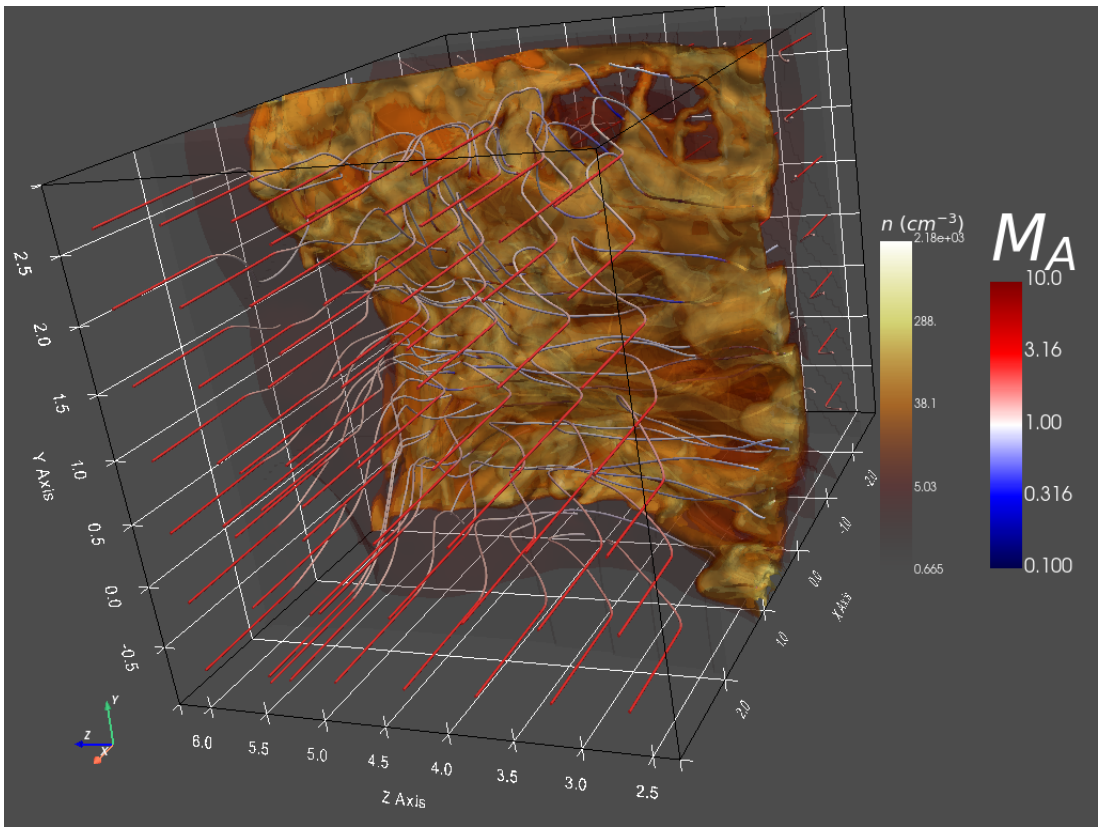

Figure 4.9: Amplification of the z component of the magnetic field in the region $x \in [0.0, 2.0]$ pc, $y \in [3.0, 6.0]$ pc, and $z \in [-1.0, 1.0]$ pc at 5 Myr. The magnetic field lines are colored by the Alfvénic Match number.

magnetic fields are aligned with the inflow, they tend to weaken or even suppress the NTSI due to the magnetic tension counteracting the transverse momentum transport. In addition, the isothermal assumption required in the analytical study of the NTSI in (Vishniac, 1994) and in the numerical approach (Heitsch et al., 2007) implies that the cooling is instantaneous, therefore the cool slab and the shock front reside in the same physical space. However, when cooling and heating processes are considered, the gas passing through the shock front condenses after a cooling time (e.g. Vázquez-Semadeni et al., 2006). Therefore, the gas flow is affected by much more complicated dynamics between the shock front and the condensed layer, which changes its trajectory and might affect the efficient momentum transport at the condensed layer. Thus the NTSI might be important only in early evolution times when the magnetic fields have not changed their orientation.

Another possible source of turbulent shear strain arises at later times in the evolution when the magnetic field lines have already been dragged and bent by the compressive velocity field, at this time the trans-Alfvénic condition of the magnetic field lines can redirect the gas flow along them, and yield the turbulent shear flow reported as the reason for the elongation and alignment of filamentary CACs. We can see one example of this situation in Figure 4.10, where the velocity fields are represented by dark arrows and the magnetic field lines are colored with the Alfvénic Match number. As we can see in this animation the troughs and peaks of CACs do not show converging and diverging velocity fields respectively as is expected in the NTSI (See Figure 2.8).

One more relevant issue related to the colliding interface is the consideration of a curved collision interface instead of a plane one. This kind of collision interface, as considered by Vishniac (1994) in the study of the NTSI, would trigger the development of this instability faster than when a plane collision interface with velocity perturbations is applied to the colliding flows three-dimensional simulation. Therefore, the momentum transfer from longitudinal to the transversal characteristic of the NTSI would be more efficient in the cold condensed layer. As a consequence, the lateral momentum could also help in the alignment of magnetic field lines with CACs.

In order to verify this, we also ran two-dimensional simulations with the same initial conditions and physics as the three-dimensional simulation described in Section 4.2 but with a curved collision interface, adding a sinusoidal displacement perturbation (a "bending mode" perturbation). In Figure 4.11, we show the initial state of this simulation where magnetic field lines are colored by the Alfvénic Match number. In this figure, we see that the field lines change their direction downstream from the curved interface not just because of the fast MHD shock, but also due to the momentum transfer characteristic of the NTSI. For this collision interface, the line bending model would be different from the one described in Section 4.4.2 because of the transfer from longitudinal to transverse momentum yield by the NTSI. In this case, we will have a velocity field like the one represented in Figure 4.12, where the left panel represents an unperturbed downstream magnetic field line and the right panel is a perturbed one. In the left panel, the line bending model considers a local system of coordinates centered at the point in which the magnetic field line, represented in green, has the greatest velocity magnitude, the x-axis is along the line, the y-axis is perpendicular to it, and the velocity field is represented by black arrows.

Thus, we have that $B_y = 0$, $B_x = C$ where C is a constant, considering u_x, $u_z \to 0$, and $u_y = u_y(x)$, we can obtain from equation (4.6)

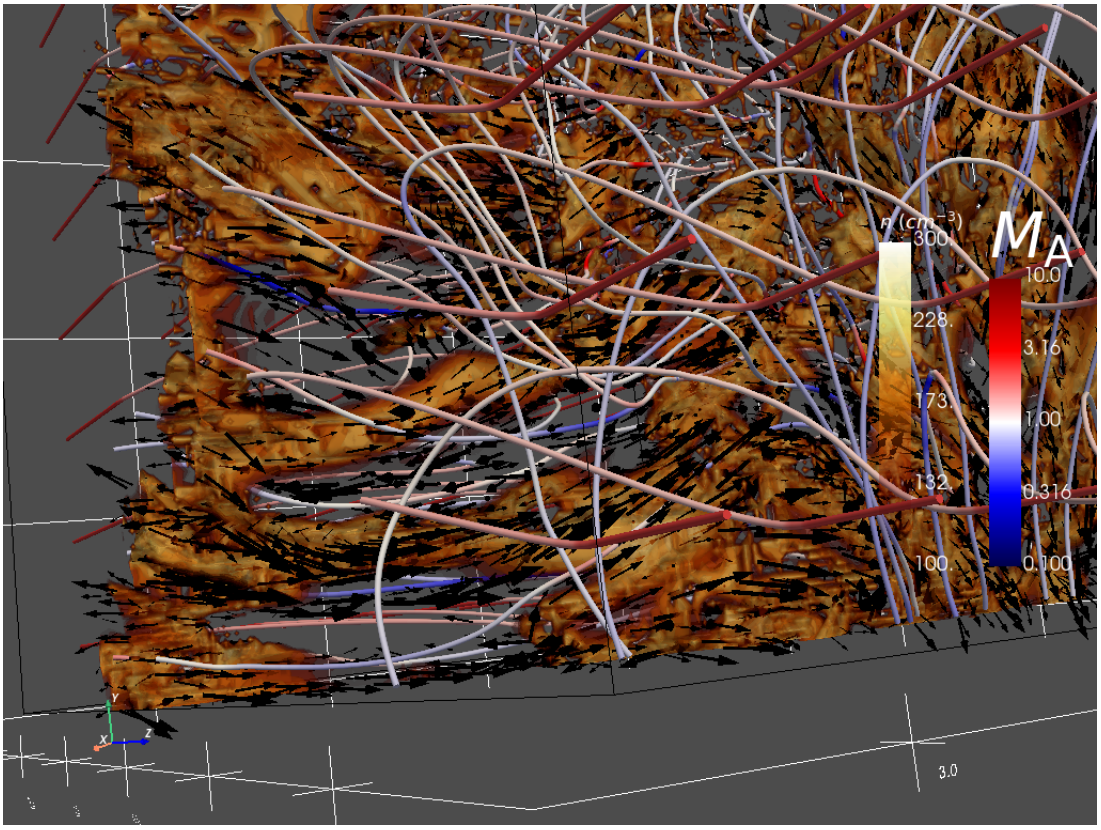

Figure 4.10: A couple of filamentary CACs located in the left-down corner. It can be seen a turbulent shear strain velocity field along their main axis and aligned with the local magnetic field. Note that the velocity field on the filamentary CACs is different from the one that would be present in the case of the NTSI (See Figure 2.8). To see the animation open this youtube link.

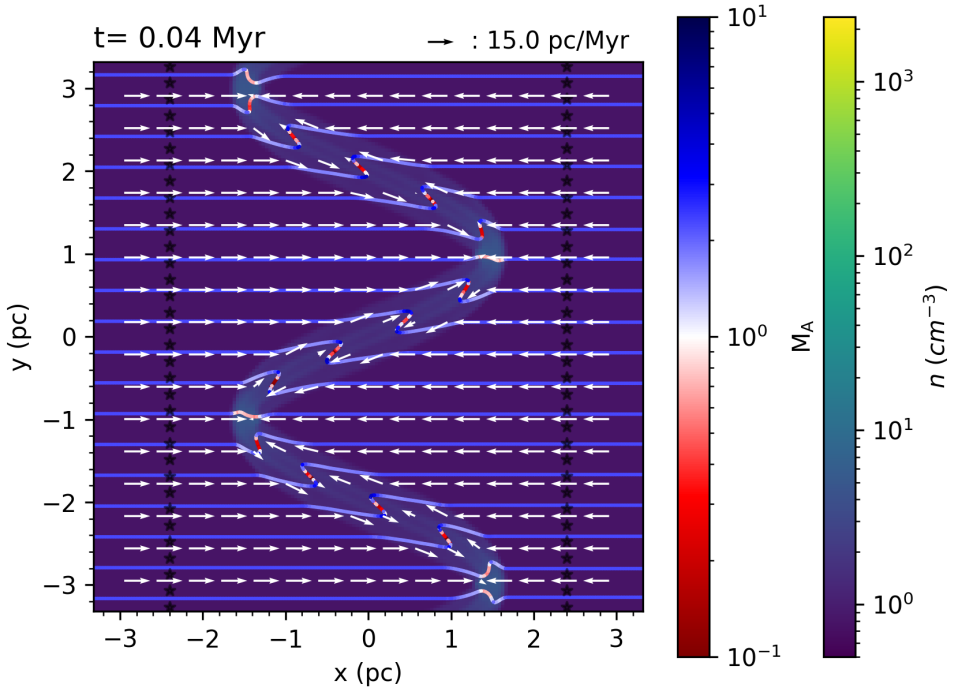

Figure 4.11: Two-dimensional simulation of warn atomic colliding flows with a curvilinear collision interface. The two color bars represent the number density and the Alfvénic Match number.

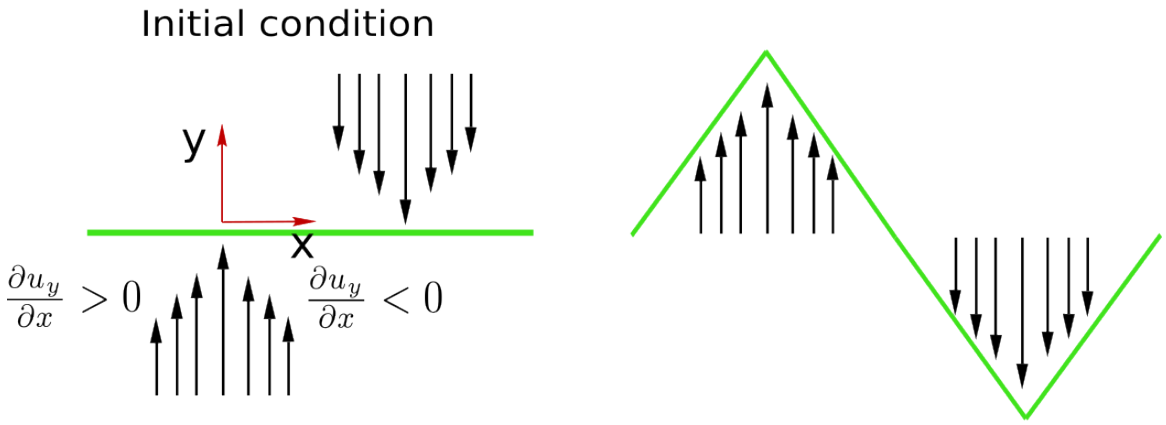

Figure 4.12: Line bending model for the colliding flows with curvilinear collision interface. The left panel represents the initial state and the right one the evolution according to the analytical model given by equation (4.9). In this sketch, the black arrows are the velocity field and the green line is a magnetic field line.

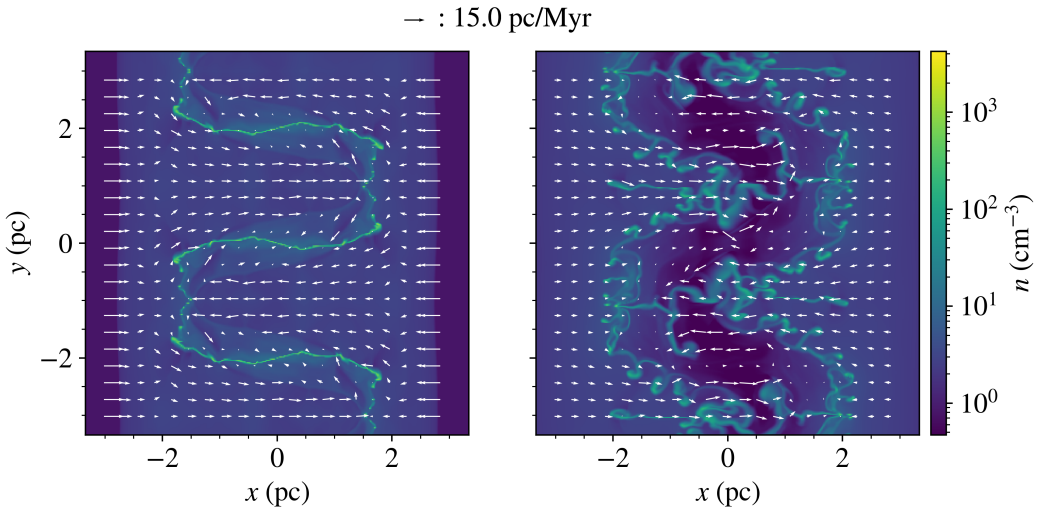

Figure 4.13: Left: Density slice of the 2D MHD simulation. Right: density slice of the 2D HD simulation. Note that for the left panel, the CACs are more filamentary than on the right panel due to the suppression of turbulence.

$$\frac{\partial B_y}{\partial t} = B_x \frac{\partial u_y}{\partial x}. \tag{4.9}$$

With this model in mind and considering the system of coordinates on the left panel of Figure 4.12, where we have two regions. First, for $x > 0$ we obtain $\partial u_y/\partial x < 0$, thus, $\partial B_y/\partial t < 0$. Second, for $x < 0$, we have $\partial u_y/\partial x > 0$, so, $\partial B_y/\partial t > 0$. Therefore, for both cases, the sign of $\partial B_y/\partial t$ explains the deformation of the magnetic field line shown in the right panel of Figure 4.12 and in Figure 4.11.

Regarding the development of the NTSI, Vishniac (1994) found that the requirement for this instability to become unstable is that the displacement of the cold slab is larger than its thickness (See equation 2.35). This condition is satisfied in the isothermal case when there is a high compression ratio across the shock, which requires that $M_s^2 \gg 1$. Our three-dimensional simulation described in Section 4.2 has $M_s^2 = 4.0$, which is not too large. Fulfilling this requirement in Vishniac (1994) is connected to achieving a high compression because in the isothermal case considered there, in which the density jump is given by $\rho_2/\rho_1 = M_s^2$. However, our simulations included the development of thermal instability induced by the cooling and heating functions described in Koyama & Inutsuka (2002). Therefore, including TI produces a much stronger compression of the condensed layer, which results in a much thinner slab dimension, so it is not difficult to fulfill the requirement for the development of the NTSI (Hueckstaedt, 2003).

It has been noticed by previous works that MHD simulations of cloud formation show more filamentary structure than pure hydrodynamical simulations due to the suppression of turbulence (e.g., Heitsch et al., 2007, 2009; Zamora-Avilés et al., 2018). To verify this, we also ran a 2D pure hydrodynamical simulation with the same initial conditions of the 2D MHD simulation as mentioned in Section 4.2. As we can see in Figure 4.13, after 3 Myr, the MHD simulation shows a more coherent filamentary structure, while the HD simulation shows a more turbulent one.

The generation of turbulence in compressed layers is due to the KH instability, which in turn is triggered by the shear flow produced by the NTSI (See Section 2.3.3) (e.g. Blondin & Marks, 1996; Heitsch et al., 2006). Therefore, a magnetic field aligned with the shear flow generated by the NTSI may suppress the development of the KHI and as a consequence the generation of turbulence. Considering that Vishniac (1994) speculated that the NTSI could form filamentary CACs, and Hueckstaedt (2003) found that cooling fuels the development of the NTSI, which triggers the KHI that disrupts the characteristic momentum transfer of the NTSI. Thus, the magnetic field would be important to suppress turbulence and allow the formation of filamentary CACs in agreement with Hennebelle (2013).

The super-Alfvénic nature of the initial inflow in our simulations that represent typical conditions of the ISM and its transition to a trans-Alfvénic flow allows the dragging and amplification of the magnetic field lines, and it is also in agreement with the observation done in Skalidis et al. (2022), where the authors explore the role of magnetic fields in the $H_I - H_2$ transition and reported trans-Alfvénic clouds.

In this work, our simulations consider only the formation of clouds by the collision of converging cold atomic flows. However, the main physical processes responsible for the alignment of magnetic field lines and density structures, MHD shocks, and the NTSI, can be also present in colliding stellar winds and supernova shells (Heitsch et al., 2007). Therefore, the MHD shocks, the compressive velocity field, and the NTSI could also be the principal physical mechanisms behind the magnetic field alignment with fibers found in Clark et al. (2014).

4.6. Summary and Conclusions

In this work, we have studied the physical mechanisms responsible for the observed alignment of magnetic field and cold atomic gravitational unbound density structures formed by the collision of converging warm atomic gas. We have tracked the evolution of magnetic field lines in a three-dimensional simulation that has typical conditions of the warm ISM and found that they become perpendicular to their original orientation and are aligned with density structures.

The process of the alignment of magnetic field lines with the density structures starts at the shock fronts where the magnetic field changes its direction due to the amplification of the magnetic field component parallel to the shock front resulting from the velocity fluctuations of the pre-shock region. This amplification occurs due to a fast MHD shock which happens when there are superfast and subfast upstream and downstream flows respectively.

When the shock front travels away from the central region it amplifies the magnetic field component parallel to the shock front which yields the initial magnetic field pattern. This initial pattern is generated by the small variation of the angle between the upstream magnetic field and the normal to the shock front due to a seed deviation in the velocity field. Afterward, the compressive downstream velocity field amplifies the magnetic field component parallel to the shock front, increasing the curvature of the lines in this region, and causing them to become increasingly parallel to the dense layer produced by the thermal instability.

We also found that under typical conditions of the ISM, the upstream flow is super-Alfvénic and becomes Trans-Alfvénic downstream. This allows the velocity field to bend and drag the magnetic field lines contrary to the usual belief that the magnetic field controls the accretion.

5

Summary and conclusions

In this Ph.D. project, we have studied two topics related to the magnetic field in the formation of clouds in the ISM. First, we proposed a resolution criterion for the solution of magnetic fields in molecular clouds based on the estimation of the characteristic timescales of the intervening physical and numerical processes. Second, we identified the physical processes responsible for the alignment of the magnetic field with cold atomic clouds.

The time-scale based resolution criterion relies on comparing the numerical magnetic diffusion time with the relevant dynamical time of the physical process under study; in the case explored in Chapter 2, the relevant dynamical time is the free-fall time. By comparing physical with numerical timescales, we aim to define resolution criteria that are physically motivated, easier to understand, and do not depend on empirical and costly convergence tests frequently used in numerical astrophysics.

To obtain the magnetic diffusion time, we conducted a numerical experiment consisting of two-dimensional MHD isothermal simulation called as Harris-like current sheet which allows the computation of the numerical magnetic diffusion coefficient at a given numerical resolution. Then, the magnetic diffusion time is obtained and compared with the free-fall time. The resolution criterion consists in finding the numerical resolution at which the dynamical time is greater than the numerical magnetic diffusion time.

The alignment of the magnetic field with cold atomic clouds was studied following the evolution of magnetic field lines in simulations of the formation of molecular clouds by colliding warm atomic gas flows. We found that under typical conditions of the interstellar medium fast shocks are generated due to the supersonic colliding flows. Fast MHD shocks amplify the upstream magnetic field component parallel to the shock front, which deviates the magnetic field lines from their original direction. When the shock front travels away from the collision surface, it generates the early downstream shocked magnetic field line pattern. Afterward, the compressive downstream velocity field amplifies the perturbed magnetic field components and drags the magnetic field lines resulting in their alignment with cold atomic clouds. Therefore, this mechanism can explain the alignment observed with dust polarization and HI emission.

We also found that the deviation in the direction of the magnetic field lines from originally perpendicular to almost parallel to the condensed layer yields shear velocity flows along them. Since shear velocity flows have been claimed as responsible for the elongation of filamentary CACs and their alignment with the local magnetic field, we have identified how this correlation takes place. In addition, we also identified another possible source of the

required shear velocity; the nonlinear thin-shell instability, which transfers longitudinal to transverse momentum and generates this kind of flow in the cold layer.

In the study of the alignment of the magnetic field with cold atomic clouds, we did not consider it necessary to apply the time-based resolution criterion for magnetic fields described in Chapter 3 because the observed evolution of magnetic field lines indicates that the influence of the numerical diffusion of the magnetic field is not important to obtain the observed alignment. Specifically, in the extreme case when magnetic diffusion dominates, the fluid and the magnetic field evolve as they were decoupled and the gas would move freely without causing any bending and dragging of the magnetic field lines, which will result in no correlation between the magnetic field and density structures.

In conclusion, this Ph.D. thesis contributes to the understanding of magnetic fields in the formation of clouds in the interstellar medium. First, by proposing a resolution criterion of magnetic fields based on the comparison of characteristic timescales. This resolution criterion, in contrast with the standard approach to control numerical diffusion using convergence tests, is physically motivated and helps to ensure the correct numerical resolution of magnetic fields. Second, we contributed to the understanding of how the magnetic field aligns density structure in the interstellar medium by finding the role played by the fast magnetohydrodynamic shock and the shear velocity field which could be longitudinal or transverse.

Acknowledgement

I would like to thank my supervisors for their dedication and willingness to review, comment and discuss many aspects related to this work. Each one of their observations and recommendations was fundamental to achieve this thesis.

Last but no least, I am grateful to my family and friends for the unconditional love and support.

Bibliography

Audit E., Hennebelle P., 2005, Astronomy and Astrophysics, 433, 1

Avila-Reese V., Vázquez-Semadeni E., 2001, The Astrophysical Journal, 553, 645

Ballesteros-Paredes J., Hartmann L. W., Vázquez-Semadeni E., Heitsch F., Zamora-Avilés M. A., 2011, Monthly Notices of the Royal Astronomical Society, 411, 65

Bate M. R., Burkert A., 1997, Monthly Notices of the Royal Astronomical Society, 288, 1060

Binney J., Tremaine S., 2008, Galactic Dynamics: Second Edition

Blitz L., Shu F. H., 1980, The Astrophysical Journal, 238, 148

Blondin J. M., Marks B. S., 1996, New Astronomy, 1, 235

Bodenheimer P., ed. 2007, Numerical Methods in Astrophysics: An Introduction. Series in Astronomy and Astrophysics, Taylor & Francis, New York

Boyd T. J. M., Sanderson J. J., 2003, The physics of plasmas. Cambridge University Press, Cambridge, UK ; New York

Chandrasekhar S., 1961, Hydrodynamic and hydromagnetic stability

Clark S. E., Peek J. E. G., Putman M. E., 2014, The Astrophysical Journal, 789, 82

Clark S. E., Hill J. C., Peek J. E. G., Putman M. E., Babler B. L., 2015, Physical Review Letters, 115, 241302

Dalgarno A., McCray R. A., 1972, Annual Review of Astronomy and Astrophysics, 10, 375

Delmont P., Keppens R., 2011, Journal of Plasma Physics, 77, 207–229

Draine B. T., 2011, Physics of the Interstellar and Intergalactic Medium. Princeton University Press

Dubey A., Reid L. B., Fisher R., 2008, Physica Scripta Volume T, 132, 014046

Dubey A., Antypas K., Ganapathy M. K., Reid L. B., Riley K., Sheeler D., Siegel A., Weide K., 2009, Parallel Computing, 35, 512

Elmegreen B. G., 2000, The Astrophysical Journal, 530, 277

Faber T. E., 1995, Fluid Dynamics for Physicists. Cambridge University Press, doi:10.1017/CBO9780511806735

Federrath C., Sur S., Schleicher D. R. G., Banerjee R., Klessen R. S., 2011, The Astrophysical Journal, 731, 62

Ferrière K. M., 2001, Reviews of Modern Physics, 73, 1031

Field G. B., 1965, The Astrophysical Journal, 142, 531

Field G. B., Goldsmith D. W., Habing H. J., 1969, The Astrophysical Journall, 155, L149

Franco J., Cox D. P., 1986, Publications of the Astronomical Society of the Pacific, 98, 1076

Fryxell B., et al., 2000, The Astrophysical Journal Supplement Series, 131, 273

Galván-Madrid R., Vázquez-Semadeni E., Kim J., Ballesteros-Paredes J., 2007, The Astrophysical Journal, 670, 480

Gerola H., Kafatos M., McCray R., 1974, The Astrophysical Journal, 189, 55

Goldreich P., Kwan J., 1974, The Astrophysical Journal, 189, 441

Granda-Muñoz G., Vázquez-Semadeni E., Gómez G. C., Zamora-Avilés M., 2022, , 510, 5062

Hartmann L., Ballesteros-Paredes J., Bergin E. A., 2001, The Astrophysical Journal, 562, 852

Heiles C., 2000, , 119, 923

Heitsch F., Burkert A., Hartmann L. W., Slyz A. D., Devriendt J. E. G., 2005, The Astrophysical Journal Letters, 633, L113

Heitsch F., Slyz A. D., Devriendt J. E. G., Hartmann L. W., Burkert A., 2006, The Astrophysical Journal, 648, 1052

Heitsch F., Slyz A. D., Devriendt J. E. G., Hartmann L. W., Burkert A., 2007, The Astrophysical Journal, 665, 445

Heitsch F., Stone J. M., Hartmann L. W., 2009, The Astrophysical Journal, 695, 248

Hennebelle P., 2013, Astronomy and Astrophysics, 556, A153

Hennebelle P., Pérault M., 1999, Astronomy and Astrophysics, 351, 309

Hennebelle P., Pérault M., 2000, Astronomy and Astrophysics, 359, 1124

Heyer M., Krawczyk C., Duval J., Jackson J. M., 2009, The Astrophysical Journal, 699, 1092

Hueckstaedt R. M., 2003, New Astronomy, 8, 295

Hunter J. H. J., Sandford M. T. I., Whitaker R. W., Klein R. I., 1986, The Astrophysical Journal, 305, 309

Inoue T., Inutsuka S.-i., 2016, The Astrophysical Journal, 833, 10

Jeans J. H., 1902, Philosophical Transactions of the Royal Society of London Series A, 199, 1

Klein R. I., Woods D. T., 1998, The Astrophysical Journal, 497, 777

Kliem B., Karlicky M., Benz A. O., 2000, Astronomy & Astrophysics, 360, 715

Koyama H., Inutsuka S.-I., 2000, The Astrophysical Journal, 532, 980

Koyama H., Inutsuka S.-i., 2002, The Astrophysical Journal Letters, 564, L97

Koyama H., Inutsuka S.-i., 2004, The Astrophysical Journal, 602, L25

Kwan J., 1979, The Astrophysical Journal, 229, 567

Larson R. B., 1969, Monthly Notices of the Royal Astronomical Society, 145, 271

Larson R. B., 1981, Monthly Notices of the Royal Astronomical Society, 194, 809

Lazarian A., Esquivel A., Crutcher R., 2012, The Astrophysical Journal, 757, 154

Leonardis A., Bischof H., Pinz A., 2006, Computer Vision – ECCV 2006: 9th European Conference on Computer Vision, Graz, Austria, May 7-13, 2006, Proceedings, Part I. Lecture Notes in Computer Science, Springer Berlin Heidelberg, https://books.google.com.mx/books?id=cTvyBwAAQBAJ

Lioure A., Chieze J. P., 1990, Astronomy and Astrophysics, 235, 379

Lohner R., 1987, Computer Methods in Applied Mechanics and Engineering, 61, 323

Mac Low M.-M., Klessen R. S., 2004, Reviews of Modern Physics, 76, 125

Mac Low M.-M., Klessen R. S., Burkert A., Smith M. D., 1998, Physical Review Letters, 80, 2754

McKee C. F., Ostriker J. P., 1977, The Astrophysical Journal, 218, 148

Meerson B., 1996, Reviews of Modern Physics, 68, 215

Mestel L., Spitzer Jr. L., 1956, Monthly Notices of the Royal Astronomical Society, 116, 503

Mouschovias T. C., 1991, in NATO Advanced Science Institutes (ASI) Series C. p. 449

Mouschovias T. C., Ciolek G. E., 1999, in NATO Advanced Science Institutes (ASI) Series C. p. 305

Naranjo-Romero R., Vázquez-Semadeni E., Loughnane R. M., 2015, The Astrophysical Journal, 814, 48

Ostriker E. C., Gammie C. F., Stone J. M., 1999a, The Astrophysical Journal, 513, 259

Ostriker E. C., Gammie C. F., Stone J. M., 1999b, The Astrophysical Journal, 513, 259

Padoan P., Nordlund Å., 1999, The Astrophysical Journal, 526, 279

Planck Collaboration et al., 2016a, Astronomy and Astrophysics, 586, A135

Planck Collaboration et al., 2016b, Astronomy and Astrophysics, 586, A138

Shu F. H., 1992, The Physics of Astrophysics. Volume II, Volume II,. University Science Books, Sausalito, Calif.

Shu F. H., Adams F. C., Lizano S., 1987, Annual Review of Astronomy and Astrophysics, 25, 23

Skála J., Baruffa F., Büchner J., Rampp M., 2015, Astronomy & Astrophysics, 580, A48

Skalidis R., et al., 2022, Astronomy and Astrophysics, 665, A77

Soler J. D., Hennebelle P., 2017, Astronomy and Astrophysics, 607, A2

Soler J. D., Hennebelle P., Martin P. G., Miville-Deschênes M. A., Netterfield C. B., Fissel L. M., 2013, The Astrophysical Journal, 774, 128

Stevens I. R., Blondin J. M., Pollock A. M. T., 1992, The Astrophysical Journal, 386, 265

Strittmatter P. A., 1966, Monthly Notices of the Royal Astronomical Society, 132, 359

Sullivan B., Kaszynski A., 2019, Journal of Open Source Software, 4, 1450

Truelove J. K., Klein R. I., McKee C. F., Holliman II J. H., Howell L. H., Greenough J. A., 1997, The Astrophysical Journal Letters, 489, L179

Turk M. J., Smith B. D., Oishi J. S., Skory S., Skillman S. W., Abel T., Norman M. L., 2011, The Astrophysical Journals, 192, 9

Vazquez-Semadeni E., Ostriker E. C., Passot T., Gammie C. F., Stone J. M., 2000, in Mannings V., Boss A. P., Russell S. S., eds, Protostars and Planets IV. p. 3 (arXiv:astro-ph/9903066), doi:10.48550/arXiv.astro-ph/9903066

Vázquez-Semadeni E., Gazol A., Passot T., et al. 2003, in Falgarone E., Passot T., eds, , Vol. 614, Turbulence and Magnetic Fields in Astrophysics. pp 213–251, doi:10.48550/arXiv.astro-ph/0201521

Vázquez-Semadeni E., Ryu D., Passot T., Gonzalez R. F., Gazol A., 2006, The Astrophysical Journal, 643, 245

Vázquez-Semadeni E., Gómez G. C., Jappsen A. K., Ballesteros-Paredes J., González R. F., Klessen R. S., 2007, The Astrophysical Journal, 657, 870

Vázquez-Semadeni E., Banerjee R., Gómez G. C., Hennebelle P., Duffin D., Klessen R. S., 2011, Monthly Notices of the Royal Astronomical Society, 414, 2511

Vázquez-Semadeni E., Palau A., Ballesteros-Paredes J., Gómez G. C., Zamora-Avilés M., 2019, Monthly Notices of the Royal Astronomical Society, 490, 3061

Vishniac E. T., 1994, The Astrophysical Journal, 428, 186

Waagan K., Federrath C., Klingenberg C., 2011, Journal of Computational Physics, 230, 3331

Wilson R. W., Jefferts K. B., Penzias A. A., 1970, The Astrophysical Journall, 161, L43

Wolfire M. G., Hollenbach D., McKee C. F., Tielens A. G. G. M., Bakes E. L. O., 1995, The Astrophysical Journal, 443, 152

Wünsch R., Walch S., Dinnbier F., Whitworth A., 2018, Monthly Notices of the Royal Astronomical Society, 475, 3393

Zamora-Avilés M., Vázquez-Semadeni E., Körtgen B., Banerjee R., Hartmann L., 2018, Monthly Notices of the Royal Astronomical Society, 474, 4824

Zuckerman B., Evans N. J. I., 1974, The Astrophysical Journall, 192, L149

Zuckerman B., Palmer P., 1974, , 12, 279

Appendix A: Magnetic diffusion coefficients for the eight-wave FLASH MHD solver

The magnetic diffusion coefficients and magnetic pressure gradients obtained for the standard FLASH MHD solver eight-wave are shown in Table 1.

These values were computed with the same procedure and initial conditions described in Section 3.4. The scaling of η for different conditions was also performed in the way described in Section 3.5.2, obtaining $\log(\eta) \approx 25.49 + 1.04 \log(|\nabla P_B|)$.

Table 1: Magnetic diffusion for the 8-wave MHD solver. The first and second columns represent the simulation name and its resolution respectively. The third and fourth columns represent numerical magnetic diffusion coefficients and magnetic pressure gradient magnitudes.

Simulation	Resolution (pc)	η (pc^2/ Myr)	$\lvert\nabla P_B\rvert$ (dyn/cm^3)
H7	7.81×10^{-2}	4.209×10^{-3}	3.289×10^{-31}
H8	3.91×10^{-2}	1.040×10^{-3}	3.400×10^{-31}
H9	1.95×10^{-2}	2.772×10^{-4}	3.389×10^{-31}
H10	9.75×10^{-3}	7.179×10^{-5}	3.378×10^{-31}
H11	4.88×10^{-3}	1.819×10^{-5}	3.371×10^{-31}

Appendix B: Magnetic field lines code

In this appendix, we provide the code used in the second part of this thesis (See chapter 3) to obtain magnetic field lines. An updated version of this code with a test data set is provided in `https://github.com/guido-granda/magnetic_field_lines`

```
import numpy as np
import h5py
from scipy.interpolate import RegularGridInterpolator

def lineas_flujo( xg, yg, zg, vx_in, vy_in, vz_in,start_points=None,outfile='lines_out.hdf5'):
    """Funtion to obtain stream lines. Input xg, yg, zg coordinates arrays with " shapes m1 , m2 , m3, vx_in,vy_in,vz_in
    vector field arrays with dimensions (m1,m2,m3), start_points logical or numpy array with dimensins (n,3) where n is the number of starting points, if it is None, it indicates if the start
    point is the center of the computational domain provided otherwise provide an array with the coordinates of the points with dimensions
    (npoints,3) where npoints is the number of points, lint  interpolation lenght. """

    #https://docs.scipy.org/doc/scipy6/reference/generated/scipy.interpolate.RegularGridInterpolator.html
    # Define forward interpolation functions
    interpol_vx_p = RegularGridInterpolator((xg, yg, zg),vx_in,bounds_error=False, fill_value=0.)
    interpol_vy_p = RegularGridInterpolator((xg, yg, zg),vy_in,bounds_error=False, fill_value=0.)
    interpol_vz_p = RegularGridInterpolator((xg, yg, zg),vz_in,bounds_error=False, fill_value=0.)
    # Define downward interpolation functions
    interpol_vx_ap = RegularGridInterpolator((xg, yg, zg),-vx_in,bounds_error=False, fill_value=0.)
    interpol_vy_ap = RegularGridInterpolator((xg, yg, zg),-vy_in,bounds_error=False, fill_value=0.)
    interpol_vz_ap = RegularGridInterpolator((xg, yg, zg),-vz_in,bounds_error=False, fill_value=0.)

    nx = len(xg)
    ny = len(yg)
    nz = len(zg)

    ## getting domain of the cube
    xmin=np.amin(xg)
    xmax=np.amax(xg)

    ymin=np.amin(yg)
    ymax=np.amax(yg)

    zmin=np.amin(zg)
```

```
    zmax=np.amax(zg)

    ds = xg[1]-xg[0] # cell size

    # Check for starting points for the magentic fields

    if start_points is not None:
        xs = start_points[:,0]
        ys = start_points[:,1]
        zs = start_points[:,2]

    else:
        xs = np.array([xg[np.int(nx/2.)]])
        ys = np.array([yg[np.int(ny/2.)]])
        zs = np.array([zg[np.int(nz/2.)]])
    #number of initial points for the lines
    npoints=len(xs)
    # Creating the hdf5 file for the output
    f=h5py.File(outfile,'w')
    f.create_dataset('nlines',data=npoints,dtype='i4')

    for i in range(npoints):
        # starting coordinates for each stream line
        xp=np.array([xs[i]])
        yp=np.array([ys[i]])
        zp=np.array([zs[i]])
        # starting fields for each stream line
        vx_ar=interpol_vx_p( np.array([xp[0],yp[0],zp[0]]) )
        vy_ar=interpol_vy_p( np.array([xp[0],yp[0],zp[0]]) )
        vz_ar=interpol_vz_p( np.array([xp[0],yp[0],zp[0]]) )


        # Forward magnetic field lines
        while ( (((xmin+ds)<xp[-1]) and (xp[-1]<(xmax-ds))) and (((ymin+ds)<yp
            [-1]) and (yp[-1]<(ymax-ds))) and (((zmin+ds)<zp[-1]) and (zp[-1]<(
            zmax-ds))) ):
            # interpolation
            vx_p = interpol_vx_p( np.array([xp[-1],yp[-1],zp[-1]]) )
            vy_p = interpol_vy_p( np.array([xp[-1],yp[-1],zp[-1]]) )
            vz_p = interpol_vz_p( np.array([xp[-1],yp[-1],zp[-1]]) )

            vel_p = np.sqrt( vx_p**2 + vy_p**2 + vz_p**2 ) + 1e-80
            dt_p  = 0.5 * ds/vel_p
            # adding forward points
            xp = np.insert( xp, len(xp), xp[-1]+vx_p*dt_p )
            yp = np.insert( yp, len(yp), yp[-1]+vy_p*dt_p )
            zp = np.insert( zp, len(zp), zp[-1]+vz_p*dt_p )

            # storing interpolated fields
            vx_ar=np.insert(vx_ar,len(vx_ar),vx_p)
            vy_ar=np.insert(vy_ar,len(vy_ar),vy_p)
            vz_ar=np.insert(vz_ar,len(vz_ar),vz_p)

        # Downward magnetic field lines
        while ( (((xmin+ds)<xp[0]) and (xp[0]<(xmax-ds))) and (((ymin+ds)<yp[0])
            and (yp[0]<(ymax-ds))) and (((zmin+ds)<zp[0]) and (zp[0]<(zmax-ds)))
```

```
            ):
86
87              # interpolation
88              vx_ap = interpol_vx_ap(np.array([xp[0],yp[0],zp[0]]))
89              vy_ap = interpol_vy_ap(np.array([xp[0],yp[0],zp[0]]))
90              vz_ap = interpol_vz_ap(np.array([xp[0],yp[0],zp[0]]))
91
92              vel_ap = np.sqrt( vx_ap**2 + vy_ap**2 + vz_ap**2 ) + 1e-80
93              dt_ap  = 0.5 * ds/vel_ap
94              # adding downward points
95              xp = np.insert( xp,0,xp[0]+vx_ap*dt_ap )
96              yp = np.insert( yp,0,yp[0]+vy_ap*dt_ap )
97              zp = np.insert( zp,0,zp[0]+vz_ap*dt_ap )
98              #downward field components
99              vx_ar=np.insert(vx_ar,0,-vx_ap)
100             vy_ar=np.insert(vy_ar,0,-vy_ap)
101             vz_ar=np.insert(vz_ar,0,-vz_ap)
102         # store all info in hdf5 file
103         grp=f.create_group('line_'+str(i))
104
105         d1=grp.create_dataset('x',data=xp)
106         d1.attrs['units']='cm'
107
108         d2=grp.create_dataset('y',data=yp)
109         d2.attrs['units']='cm'
110
111         d3=grp.create_dataset('z',data=zp)
112         d3.attrs['units']='cm'
113
114         d4=grp.create_dataset('x␣point',data=xs)
115         d4.attrs['units']='cm'
116
117         d5=grp.create_dataset('y␣point',data=ys)
118         d5.attrs['units']='cm'
119
120         d6=grp.create_dataset('z␣point',data=zs)
121         d6.attrs['units']='cm'
122
123         d7=grp.create_dataset('Bx',data=vx_ar)
124         d7.attrs['units']='uG'
125
126         d8=grp.create_dataset('By',data=vy_ar)
127         d8.attrs['units']='uG'
128
129         d9=grp.create_dataset('Bz',data=vz_ar)
130         d9.attrs['units']='uG'
131
132         d10=grp.create_dataset('B',data=np.sqrt(vx_ar**2+vy_ar**2+vz_ar**2))
133         d10.attrs['units']='uG'
134
135     f.close()
```